Finite Element Methods for Large-Strain Poroelasticity/Chemotaxis Models Simulating the Formation of Myocardial Oedema

N. A. Barnafi[1] · **B. Gómez-Vargas**[2] · **W. J. Lourenço**[3] · **R. F. Reis**[3] · **B. M. Rocha**[3] · **M. Lobosco**[3] · **R. Ruiz-Baier**[4,5,6] · **R. Weber dos Santos**[3]

Abstract

In this paper we propose a novel coupled poroelasticity-diffusion model for the formation of extracellular oedema and infectious myocarditis valid in large deformations, manifested as an interaction between interstitial flow and the immune-driven dynamics between leukocytes and pathogens. The governing partial differential equations are formulated in terms of skeleton displacement, fluid pressure, Lagrangian porosity, and the concentrations of pathogens and leukocytes. A five-field finite element scheme is proposed for the numerical approximation of the problem, and we provide the stability analysis for a simplified system emanating from linearisation. We also discuss the construction of an adequate, Schur complement based, nested preconditioner. The produced computational tests exemplify the properties of the new model and of the finite element schemes.

1 Introduction

Poroelastic structures are found in many applications of industrial and scientific relevance. Examples include the interaction between soft permeable tissue and blood flow, and the study of biofilm growth and distribution near fluids (see [34, 71]). Recent applications of poroelastic consolidation theory to the poromechanical characterisation of soft living tissues relate with oxygen diffusivity in cartilage [54], swelling of hydrogels [83], feather and scale development [10], tumour localisation and biomass growth [70], cardiac perfusion [11, 24, 30], chemically-controlled cell motion [56], lung characterisation [14], traumatic brain injury

---

✉ R. Ruiz-Baier
  ricardo.ruizbaier@monash.edu

Extended author information available on the last page of the article

🌀 Springer

[32], the formation of inflammatory oedema in the context of blood-brain barrier failure [50], and immune systems for small intestine [75, 82] as well as for myocarditis [39].

In this work we are concerned with the latter application involving the formation and evolution of oedema, a build up of excess of fluid content in the intercellular space, in myocardial tissue. Local infection of tissue by pathogens contribute to an inflammatory reaction driven by the immune system with the aim of protecting the compromised region against invading organisms. Driven by oncotic and hydrostatic pressure gradients, there is a transvascular water flux: capillaries transport fluid into and out from the interstitium (the intercellular region), and lymphatic nodes contribute to returning fluid out from that space. This work also considers that, before infection occurs, the body is under osmotic equilibrium since the capillary barrier is permeable to ions. In this case, ions have no significant effect on the interstitial flow under normal conditions, otherwise, a previous disease may exist. The presence of pathogens inside a cell as well as tissue damage caused by them may change this scenario, i.e., ion-concentration may change, impacting local pressure. However, in this work, we assume, for simplification purposes, that the main cause of oedema formation is the presence of the pathogen in the tissue and the immune response to it. In the process of inflammatory response, local vasodilation occurs, which not only allows leukocytes to leave the bloodstream and to access the infection site but also increases the accumulation of fluid in the intercellular space, see Fig. 1. However such abnormal accumulation of interstitial fluid content may lead to local stress generation, tissue deformation and swelling, eventually producing a number of complications that can impair the normal function of the tissue. Oedema may be found in several types of tissue. Heart oedemas are commonly observed in myocarditis and they constitute one of the main criteria used in medical practice to its diagnosis [41, 62]. Deriving refined continuum-based models for cardiac oedema formation valid in the large strain regime and that include 3D personalised geometries have the potential to describe mechanistic processes that are observable by clinical evidence and to provide deeper insight into the complex multiscale mechanisms that are inherent to the impairing of the healthy cardiovascular function.

We extend the preliminary results from [39, 40] and develop a simplified phenomenological model for the dynamic interaction between poroelastic finite strain deformations and the chemotaxis of leukocytes towards pathogens. The present framework assumes that the porous skeleton admits heterogeneities at the macro scale, and that the pores are all interconnected. We also consider that inertial forces are negligible. The solid-fluid interaction describing the distribution of flow within the deformable skeleton is then cast in Lagrangian coordinates using the solid displacement, the fluid pressure, and the nominal porosity (ratio between the pore volume and the total volume), whereas the immune system dynamics are represented by the concentrations of leukocytes and a pathogen. The model for the immune system has also been modified to better represent the dynamics that occur after the pathogen has been eliminated. Furthermore, the mechanical feedback into pathogens and leukocyte populations are now taken into account, and we have explored these aspects further in our recent work [52], which uses the present formulation for the coupled poromechanical/chemotaxis equations.

Even if many numerical methods for the approximation of linear poroelasticity and their convergence analysis can be found in the recent literature (see [12, 17–19, 55] and the references therein), much less attention has been given to formulations addressing large-strain poromechanics. In this regard, recent works include an enriched Galerkin framework [27], stabilised finite elements [15, 84] and hybrid finite elements as well [83]. Although most contributions address the problem in a Lagrangian frame of reference, some alternative formulations include descriptions in Eulerian [65] and ALE [22] coordinates. Besides the stress response, nonlinear models differ from the linear ones in that pressure is not a primary

variable, but instead it is given by constitutive modelling [25, 31]. Instead, we follow the framework of [30, 53] (and other similar models) where the issue is circumvented through solid phase incompressibility, which yields a Lagrange multiplier acting as hydrostatic pressure.

The extension of such solution techniques for large scale simulations is highly non-trivial due to the requirement of efficient preconditioned iterative methods for the poroelasticity problem. Preconditioning strategies are mainly given by operator preconditioning [9, 46] and block factorisations [42, 79]. In this regard, block preconditioners are more easily generalisable, but an efficient implementation requires an adequate approximation of the Schur complement, usually approximated through a fixed-stress formulation in poroelasticity [38, 42, 79]. Despite all of this, an efficient numerical solver for a linearisation of large-strain poromechanics with nominal porosity as a primary variable remains largely unaddressed.

In the present case we formulate the set of nonlinear equations using as primary variables the solid displacement, the fluid pressure, the Lagrangian porosity, and the concentrations of leukocytes and pathogens. A finite element method is employed for the space discretisation [67], combined with a first-order backward Euler time advancing scheme. The method uses a MINI element for the displacement-porosity pair [6] (see also [8, 23] for the case of hyperelasticity), and linear Lagrangian elements for the remaining unknowns. As the stability of the fully nonlinear system is still a paramount task (and an open problem even for the segregated nonlinear poroelasticity without the reaction-diffusion coupling, see, e.g., [12]), we address the solvability of the linearised set of equations, focusing on the semidiscrete in-time formulation. For the corresponding analysis, we propose a fixed-point strategy, and then, Schauder fixed point theorem, together with the Fredholm alternative, the Babuška–Brezzi theory, the Lax–Milgram lemma, and classical theory of quasi-linear equations, allow us to assert unique solvability robustly with respect to the material parameters of the linearised poroelastic solid. Then, we address the numerical approximation of the linearised problem through a Krylov subspace method with a Schur complement preconditioner.

The main advantages of the proposed mathematical model and the associated computational methods are i) a consistent theoretical framework valid for finite strains that stems as the natural generalisation of three-field linear poroelasticity from [60] (which is written in terms of displacement, fluid pressure, and *total pressure*), ii) the versatility of the formulation to accommodate 2D or 3D geometries, iii) the accuracy of the numerical scheme and efficiency of the Krylov subspace iterative methods under consideration, and iv) the potential of the methodology in replacing current invasive methods for the detection of interstitial fibrosis and myocarditis (such as endo-myocardial biopsy) by techniques hinging only on MRI data.

We have organised the contents of this paper in the following manner. Section 2 outlines the main details of the model problem, motivating each component in the balance equations and stating main assumptions together with typical boundary conditions. In Sect. 3 we present the weak formulation of the nonlinear coupled problem, as well as the derivation of the linearised form of the weak formulation. Then, in Sect. 4, we address the solvability of the linearised set of equations. Section 5 contains the derivation of a finite element scheme, including the fully discrete problem in matrix form, and we address the construction of efficient solvers tailored for the multiphysics coupled system. In Sect. 6 we present a number of computational results, consisting in a simple numerical study concerning the sensitivity analysis of relevant model parameters, the verification of spatio-temporal convergence, and an investigation of different cases on simplified and physiologically accurate geometries. We close with some remarks and a discussion on model extensions collected in Sect. 7.

2 Continuum Model and Proposed Set of Field Equations

The different scales and structural components in the tissue suggest to employ a continuum model. We assume that the tissue is a poroelastic medium with interstitial fluid completely filling the void spaces. Adopting usual kinematic conventions and notation, let us consider a domain $\Omega \subset \mathbb{R}^d$, $d = 2, 3$ representing the volume occupied by a deformable porous structure in its reference configuration. We will denote by $\boldsymbol{n}$ the outward unit normal vector on the boundary $\partial \Omega$. We also disjointly partition the boundary into the sub-boundaries Γ and Σ (also in the reference undeformed state) where different types of boundary conditions, associated with the equations of motion, will be applied. A material particle in the undeformed domain Ω is identified by its position $\boldsymbol{x}$ (and, unless specified otherwise, all differential operators such as gradients and divergences will be evaluated with respect to these undeformed coordinates), whereas $\boldsymbol{u} : \Omega \to \mathbb{R}^d$ will denote the displacement field defining its new position $\boldsymbol{x} + \boldsymbol{u}$ in the deformed configuration. The tensor $\mathbf{F} := \mathbf{I} + \nabla \boldsymbol{u}$ is the gradient (applied with respect to the fixed material coordinates) of the deformation map and $\mathbf{I}$ denotes the identity tensor; its Jacobian determinant, denoted by $J = \det \mathbf{F} = \det(\mathbf{I} + \nabla \boldsymbol{u})$, measures the dilation (solid volume change during the deformation); and $\mathbf{C} = \mathbf{F}^t \mathbf{F}$ is the right Cauchy–Green deformation tensor, where the superscript $()^t$ denotes the transpose operator.

The non-viscous filtration flow through the non-deformed porous skeleton can be described by Darcy's law [2, 3]. Adopting its parabolic formulation solely in terms of pressure head (which condenses momentum and mass conservation equations for the fluid) and combining it with the conservation of linear momentum in the solid, we obtain the extension of Biot consolidation equations to the regime of large strains. This can be carried out using the descriptions already available in, e.g., [15, 53, 84]. In this paper we choose to write them using the first Piola–Kirchhoff stress tensor $\mathbf{P} = \mathbf{P}_{\text{eff}} - \alpha p J \mathbf{F}^{-t}$ and the effective (hyperelastic) stress $\mathbf{P}_{\text{eff}} = \frac{\partial \Psi_s}{\partial \mathbf{F}}$. For incompressible neo–Hookean and Holzapfel–Ogden solids one has the following forms (see, e.g., [45, 63])

$$\Psi_s^{\text{NH}}(\mathbf{C}) = \frac{\mu_s}{2}(I_1(\mathbf{C}) - d),$$
$$\Psi_s^{\text{HO}}(\mathbf{C}) = \frac{a}{2b}e^{b(I_1(\mathbf{C})-d)} + \frac{a_{fs}}{2b_{fs}}\big[e^{b_{fs}I_{8,fs}(\mathbf{C})^2} - 1\big] + \sum_{i\in\{f,s\}}\frac{a_i}{2b_i}\big[e^{b_i(I_{4,i}(\mathbf{C})-1)_+^2} - 1\big],$$

$$(2.1)$$

respectively, where μ_s, a, b, a_i, b_i with $i \in \{f, s, fs\}$ are material parameters and we have used the notation $(\zeta)_+ := \zeta$ if $\zeta > 0$ or zero otherwise, and the invariants and pseudo-invariants of $\mathbf{C}$ measuring isotropic and direction-specific stretches $I_1(\mathbf{C}) = \text{tr } \mathbf{C}$, $I_{4,f}(\mathbf{C}) = \boldsymbol{f}_0 \cdot (\mathbf{C}\boldsymbol{f}_0)$, $I_{4,s}(\mathbf{C}) = \boldsymbol{s}_0 \cdot (\mathbf{C}\boldsymbol{s}_0)$, $I_{8,fs}(\mathbf{C}) = \boldsymbol{f}_0 \cdot (\mathbf{C}\boldsymbol{s}_0)$. Here $\boldsymbol{f}_0$ and $\boldsymbol{s}_0$ denote local alignment of fibres and sheetlets which is inherent to the local microstructure of the myocardial tissue [58]. Histological studies based on diffusion tensor imaging indicate a fibre architecture that rotates $120°$ from the epicardial to the endocardial surface. A volumetric part of the energy is added for the case of nearly incompressible materials, for example, the term $U(J) = \frac{1}{2}\lambda_s(\ln J)^2$ (with λ_s another material parameter) which is designed to enforce convexity or polyconvexity of the strain density [85].

Provided that the volumetric stiffness of the solid is substantially smaller than that of the constituent (which is reasonable for soft living tissues, see, e.g., [50, 54]), volume changes of solid constituent are negligible, implying that

$$J = 1 + \phi_f - \phi_0,$$

where $\phi_f - \phi_0$ is the nominal porosity change in the reference configuration [53] (here we are assuming that the mixture is saturated, that is, $\phi_f + \phi_s = 1$, where ϕ_s is the volume fraction of the solid). Recall that the Lagrangian porosity is the natural state variable being work-conjugate to the fluid pressure p (see, e.g., [59]). Should pre-stress be considered, we need to take instead $J = J_0 + \phi_f - \phi_0$, where J_0 is the volume associated with the pre-stress. Note that the specific form of the strain energy density Ψ_s is considered irrespective of the fluid saturating the solid. It can also be derived from subtracting the volumetric free energy of the fluid from the total Helmholtz free energy of the mixture $\Psi_s = \Psi - \phi_f \Psi_f$, where ϕ_f is the nominal (Lagrangian) porosity measuring the current fluid volume per unit reference total volume [59, 84]. Note also that rearrangement of tissue components as a result of change in fluid content will imply an additional solid deformation as well as a stress modification [27, 50, 61].

The problem is then stated in a Lagrangian framework and in terms of the solid displacement $\boldsymbol{u}$, the fluid pressure p, and the nominal porosity ϕ_f, as

$$-\mathbf{Div}[\mathbf{P}_{\text{eff}} - \alpha p J \mathbf{F}^{-\mathsf{t}}] = \rho_s \boldsymbol{b} \qquad \text{in } \Omega \times (0, t_{\text{final}}], \quad (2.2a)$$

$$\rho_f D_t \phi_f - \frac{1}{J} \, \mathrm{Div}\left(\phi_f \rho_f J \mathbf{F}^{-1} \frac{\boldsymbol{\kappa}(J, \phi_f)}{\mu_f} \mathbf{F}^{-\mathsf{t}} \nabla p\right) = \rho_f \ell \qquad \text{in } \Omega \times (0, t_{\text{final}}], \quad (2.2b)$$

$$J - \phi_f = 1 - \phi_0 \quad \text{in } \Omega \times (0, t_{\text{final}}], \quad (2.2c)$$

where Div and **Div** are the divergence operators (with respect to the coordinates in the reference configuration) for vector and tensor fields, respectively. Equation (2.2a) is the balance of linear momentum for the multiphase system expressed in terms of the true total stress; (2.2b) states the mass conservation (or continuity) of fluid content in a material framework, written in terms of the nominal flux that includes the movement of the fluid phase due to pressure gradient under Darcy's law (which in particular discards shear flow effects and is valid for small Reynolds numbers); and (2.2c) represents the aforementioned kinematic constraint relating volume and porosity. It states the material incompressibility of the constituents, but it still allows for compression of the medium since the pore volume can change locally in connection with modifications in the macroscopic mass density of the poroelastic material. A more complete discussion can be found in [53]. This description is independent of the material constitutive model for the solid matrix, and the balance of angular momentum simply furnishes the condition $\mathbf{F}\mathbf{P}^{\mathsf{t}} = \mathbf{P}\mathbf{F}^{\mathsf{t}}$. Here D_t indicates the material time derivative (with respect to skeleton particles), $\boldsymbol{b}$ is a vector of external body loads, ℓ is a distributed source/sink strength term (local source volume of fluid added per volume of tissue per unit time) that accounts for fluid being added or removed from the interstitium by the blood and lymph capillaries and its specific form will be made precise later on, ρ_s is the reference density of the porous matrix, ρ_f is the reference density of the interstitial fluid, α is the Biot–Willis modulus assuming values between 0 and 1, and μ_f is the dynamic viscosity of the interstitial liquid.

The porosity-dependent heterogeneous tensor of intrinsic permeability (or hydraulic conductivity) $\boldsymbol{\kappa}$ can be defined by using normalised Kozeny–Carman (KC), exponential (E), or by power-law (PL) relations defined, respectively, as

$$\boldsymbol{\kappa}_{\text{iso}}^{\text{KC}}(J, \phi_f) = \kappa_0 \mathbf{I} + \frac{\kappa_0}{\phi_0^3}(1 - \phi_0)^2 J \phi_f^3 (J - \phi_f)^2 \mathbf{I},$$

$$\boldsymbol{\kappa}_{\text{iso}}^{\text{E}}(J, \phi_f) = \kappa_0 \left(\frac{J - \phi_f^3}{1 - \phi_f^3}\right)^3 \exp(M_0(J^2 - 1)/2)\mathbf{I}, \quad \boldsymbol{\kappa}_{\text{iso}}^{\text{PL}}(J, \phi_f) = \kappa_0 \left(\frac{J\phi_f}{\phi_0}\right)^{2/3} \mathbf{I},$$

where $\kappa_0 = d_m^2 \phi_0^3 / 180(1 - \phi_0)^2$, d_m is the typical diameter of pores or of solid grains, and M_0 is the slope of the normalised permeability curve [7, 14, 84]. As porosity is a volumetric quantity, these forms of permeability are isotropic and therefore indifferent to rotation and shear effects. A relatively simple phenomenological extension that accommodates anisotropy due to tissue microstructure is given as follows (using as example the Kozeny–Carman law)

$$\boldsymbol{\kappa}^{\text{KC}}(J, \phi_f) = \kappa_0 \left(1 + \frac{1}{\phi_0^3}(1 - \phi_0)^2 J \phi_f^3 (J - \phi_f)^2\right) \left(\frac{\kappa_{f_0}}{I_{4,f}} \mathbf{F} \boldsymbol{f}_0 \otimes \mathbf{F} \boldsymbol{f}_0 + \frac{\kappa_{s_0}}{I_{4,s}} \mathbf{F} \boldsymbol{s}_0 \otimes \mathbf{F} \boldsymbol{s}_0\right),$$
(2.3)

where $\kappa_{f_0}, \kappa_{s_0}$ are weights for the principal hydraulic conductivities such that the ratio $\kappa_{f_0}/\kappa_{s_0} \approx 2.5$ coincides with the anisotropy ratio typically used for the conductivity tensor in the extracellular domain of bidomain models [29, 74] (and much milder than the ratio observed in the intracellular domain, or in other porous skeletons such as sand or cartilage [21, 37]). This allows to reproduce the preferential perfusion direction of the micro-vascular system following the orientation of cardiac fibres $\boldsymbol{f}_0, \boldsymbol{s}_0$. Other transformations that go beyond the kinematic nonlinearity induced by change of frame can be found in models exploiting strain-dependence [7] or stress-assistance mechanisms [26]. Unless otherwise specified, we will use (2.3).

The infection process starts when an invader (pathogen) enters the poroelastic tissue. Once there, it starts to propagate. The exact mechanism adopted for increasing the pathogen population (replication, in the case of viruses, or reproduction, otherwise) is not essential to our model. In our simplification, γ_p represents the rate at which the pathogen propagates.
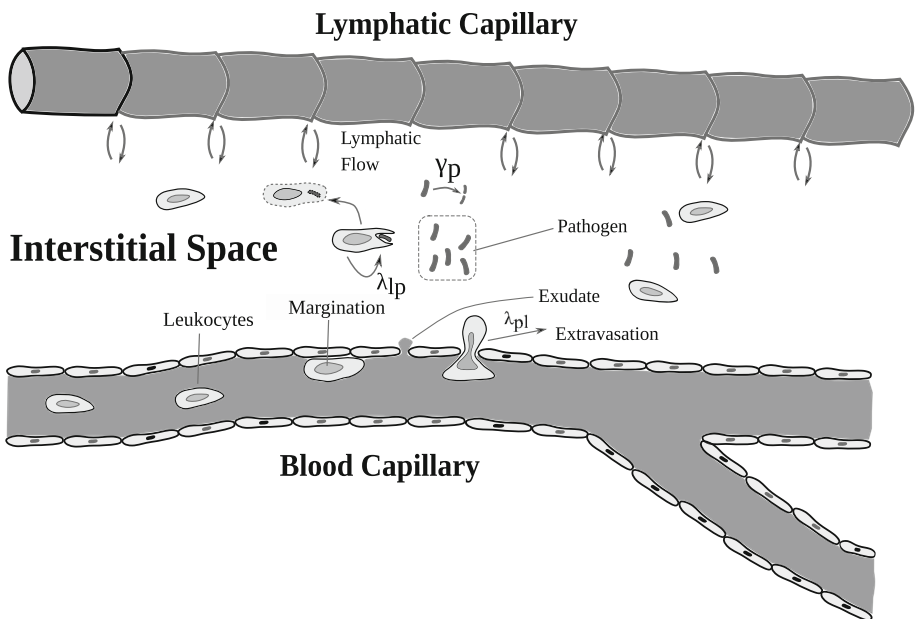

Fig. 1 Sketch of local infection of tissue by pathogens, triggering inflammatory and immune responses. In the inflammatory response process, local increment vascular permeability occurs, which allows leukocytes to leave the bloodstream to access the infection site which also leads to fluid accumulation in the interstitial space. Driven by oncotic and hydrostatic pressure gradients, blood capillaries transport fluid into and out of the interstitium, and lymphatic capillaries contribute to the resolution of the oedema

The innate immune cells (leukocytes) use their receptors to sense the presence of non-self molecules characteristic of pathogens. After the presence of pathogens is identified, leukocytes start to produce pro-inflammatory cytokines, which increase vascular permeability and recruit more leukocytes to the site of infection. The model does not include cytokines because the concentration of pathogens and leukocytes can indirectly represent their effect on vascular permeability and recruitment of leukocytes. Additionally, we assumed a simplified reaction term for the leukocytes since among these cells some have a very long life span when compared to the timescale of the simulations considered in this work. For example, macrophages can live from months to years [76]. Evidently, leukocyte death from apoptosis and pathogen phagocytosis create a sink that was not considered in the current work. Leukocytes adhere to the endothelial cells that line the vessels, a phenomenon called margination (Fig. 1). The increase in vascular permeability facilitates leukocyte extravasation to the tissue. The model considers that leukocytes leave the bloodstream to the tissue with an extravasation rate equals to λ_{pl}. The leukocytes move towards the site of infection due to the presence of chemoattractants. The chemotactic rate is given by χ_{cl}. Finally, leukocytes can start the phagocytosis of pathogens, eliminating them at a rate equal to λ_{lp} (Fig. 1). We denote by c_p and c_l the concentrations of pathogens and leukocytes, respectively. Both populations can also diffuse in the interstitial fluid. Their dynamics, in the current configuration and with derivatives in terms of the deformed coordinates, are governed by

$$\partial_t(\phi_f c_p) + \left(\partial_t \boldsymbol{u} - \frac{\kappa}{\mu_f}\nabla p\right)\cdot\nabla c_p - \text{div}(\mathbf{D}_p\nabla c_p) = r_p(\phi_f, c_p, c_l) \text{ in } \Omega_t \times (0, t_{\text{final}}],$$

$$\partial_t(\phi_f c_l) + \left(\partial_t \boldsymbol{u} - \frac{\kappa}{\mu_f}\nabla p\right)\cdot\nabla c_l - \text{div}(\mathbf{D}_l\nabla c_l - \chi c_l\nabla c_p) = r_l(\phi_f, c_p, c_l) \text{ in } \Omega_t \times (0, t_{\text{final}}],$$

where $\mathbf{D}_l$, $\mathbf{D}_p$ are positive-definite diffusion tensors for the species within the interstitial fluid, and r_l, r_p are reaction terms adopting the following specific forms (see, e.g., [39])

$$r_p(\phi_f, c_p, c_l) = \phi_f(\bar{\gamma}_p - \bar{\lambda}_{lp}c_l)c_p, \quad r_l(\phi_f, c_p, c_l) = \bar{\lambda}_{pl}\phi_f c_p c_l,$$

with $\bar{\gamma}_p$, $\bar{\lambda}_{lp}$, and $\bar{\lambda}_{pl}$ being constant coefficients (pathogen growth rate, leukocyte phagocytosis rate, and leukocyte migration rate, respectively) [39]. Note that the advecting velocity corresponds to the filtration velocity (that between the solid and fluid velocities, as the species are supposed to be transported in the interstitial fluid). Pulling back these advection-reaction-diffusion equations to the reference frame we obtain a modified system with kinematic nonlinearity

$$D_t(\phi_f c_p) - \frac{1}{J}\text{Div}(\phi_f J\mathbf{F}^{-1}\mathbf{D}_p\mathbf{F}^{-t}\nabla c_p) = r_p(\phi_f, c_p, c_l) \text{ in } \Omega \times (0, t_{\text{final}}], \tag{2.4a}$$

$$D_t(\phi_f c_l) - \frac{1}{J}\text{Div}(\phi_f J\mathbf{F}^{-1}\mathbf{D}_l\mathbf{F}^{-t}\nabla c_l - \chi\phi_f c_l J\mathbf{F}^{-1}\mathbf{F}^{-t}\nabla c_p) = r_l(\phi_f, c_p, c_l) \text{ in } \Omega \times (0, t_{\text{final}}]. \tag{2.4b}$$

Note that, in order to make the advection completely absorbed by the total derivative we have considered the total fluid-solid velocity. In turn, this implies that we are assuming that pathogens and leukocytes are able to move in the solid also.

Next we return to the continuity Eq. (2.2b) to specify the source (rate of fluid movement) ℓ. This term will encode the immune response feedback into the hydromechanics by setting a Starling-Hill function of the type

$$\ell(p, c_p) = c_f(c_p)[p_c - p - \sigma(c_p)(\pi_c - \pi_i)] - \ell_0\left[1 + \frac{v_{\text{max}}(p - p_0)^n}{k_m^n + (p - p_0)^n}\right],$$

specified by the nonlinear functions of the pathogen concentration (capillary conductivity and reflection coefficient, respectively)

$$c_f(c_p) = (S/V)L_{p0}(1 + L_{bp}c_p), \qquad \sigma(c_p) = \sigma_0(1 + L_{br}c_p)^{-1}.$$

The remaining coefficients $\ell_0, p_c, \pi_c, \pi_i, v_{\max}, k_m, n, p_0, S/V, L_{p0}, L_{bp}, L_{br}$ (normal lymph flow, capillary basal pressure, capillary oncotic pressure, interstitial oncotic pressure due to plasma protein, maximal lymph flow, half-live of pressure to lymph flow, Hill coefficient, normal interstitial fluid pressure, vessel area per volume unit, healthy tissue hydraulic permeability of the capillary wall, intensity of the pathogen infection into permeability, and influence of pathogens in the reflection coefficient; respectively) are positive model constants [39].

To close the system composed by (2.2a)–(2.2c) and (2.4a)–(2.4b), we need to provide suitable initial data and boundary conditions. We suppose that the system is initially at rest and with an homogeneous distribution of the leukocytes and pathogens in the domain

$$\phi_f(0) = \phi_0, \quad p(0) = 0, \quad \boldsymbol{u}(0) = \boldsymbol{0}, \quad c_l(0) = c_{l,0}, \quad c_p(0) = c_{p,0} \quad \text{in } \Omega. \quad (2.5)$$

In addition, on the boundaries Γ and Σ we prescribe zero traction and displacement, respectively; and zero flux everywhere on the boundary for the species interacting in the immune system. That is, we consider the following set of boundary conditions

$$\boldsymbol{u} = \boldsymbol{0}, \quad \text{and} \quad \phi_f J \mathbf{F}^{-1} \frac{\kappa(J, \phi_f)}{\mu_f} \mathbf{F}^{-\mathsf{t}} \nabla p \cdot \boldsymbol{n} = 0 \qquad \text{on } \Gamma \times (0, t_{\text{final}}], \quad (2.6a)$$

$$\mathbf{P}\boldsymbol{n} = J \mathbf{F}^{-\mathsf{t}} \boldsymbol{t}_\Sigma, \quad \text{and} \quad p = p_0 \qquad \text{on } \Sigma \times (0, t_{\text{final}}], \quad (2.6b)$$

$$\phi_f J \mathbf{F}^{-1} \mathbf{D}_p \mathbf{F}^{-\mathsf{t}} \nabla c_p \cdot \boldsymbol{n}$$
$$= [\phi_f J \mathbf{F}^{-1} \mathbf{D}_l \mathbf{F}^{-\mathsf{t}} \nabla c_l - \chi \phi_f c_l J \mathbf{F}^{-1} \mathbf{F}^{-\mathsf{t}} \nabla c_p] \cdot \boldsymbol{n} = 0 \qquad \text{on } \partial\Omega \times (0, t_{\text{final}}], \quad (2.6c)$$

where $\boldsymbol{t}_\Sigma$ is a given boundary traction applied in the current configuration.

3 Weak Formulation and Consistent Linearisation

We derive a weak form for the coupled system, carry out a Newton–Raphson linearisation, and then discuss the solvability of a simplified system arising from the linearisation with respect to conditions at rest. That resulting problem coincides in structure with the coupled Biot/reaction-diffusion equations.

3.1 General Weak form and in-time Discretisation

In view of the essential boundary conditions for displacement and fluid pressure (2.6a) and (2.6b), we define the Hilbert spaces

$$\mathbf{H}^1_\Gamma(\Omega) = \{\boldsymbol{v} \in \mathbf{H}^1(\Omega) : \boldsymbol{v}|_\Gamma = \boldsymbol{0}\}, \quad \mathrm{H}^1_\Sigma(\Omega) = \{q \in \mathrm{H}^1(\Omega) : q|_\Sigma = 0\},$$

associated with the classical norms in $\mathbf{H}^1(\Omega)$, and $\mathrm{H}^1(\Omega)$, respectively. The nonlinear weak form of the equations of motion and of the transport for the immune system can be established following a standard approach, that is, multiplying each field equation by a suitable test function, integrating over Ω, and invoking the divergence theorem whenever appropriate. To lighten the presentation, we drop the measures $d\boldsymbol{x}$ and $d\mathrm{s}$ from the integrals, which are to be understood throughout the manuscript as the Lebesgue measure. This leads to the following

continuous, five-field weak formulation: For almost all $t > 0$, find $(c_p, c_l) \in [H^1(\Omega)]^2$, $\boldsymbol{u} \in \mathbf{H}_\Gamma^1(\Omega)$, $p \in H_\Sigma^1(\Omega)$, and $\phi_f \in L^2(\Omega)$, such that

$$\int_\Omega J D_t(\phi_f c_p) w_p + \int_\Omega \phi_f J \mathbf{F}^{-1} \mathbf{D}_p \mathbf{F}^{-t} \nabla c_p \cdot \nabla w_p$$

$$= \int_\Omega J r_p(\phi_f, c_p, c_l) w_p \qquad \forall w_p \in H^1(\Omega),$$

$$\int_\Omega J D_t(\phi_f c_l) w_l + \int_\Omega \phi_f J \mathbf{F}^{-1} (\mathbf{D}_l \mathbf{F}^{-t} \nabla c_l - \chi c_l \mathbf{F}^{-t} \nabla c_p) \cdot \nabla w_l$$

$$= \int_\Omega J r_l(\phi_f, c_p, c_l) w_l \qquad \forall w_l \in H^1(\Omega),$$

$$\int_\Omega (\mathbf{P}_{\text{eff}} - \alpha p J \mathbf{F}^{-t}) : \nabla \boldsymbol{v} - \int_\Sigma J \mathbf{F}^{-t} \boldsymbol{t}_\Sigma \cdot \boldsymbol{v}$$

$$= \int_\Omega \rho_s \boldsymbol{b} \cdot \boldsymbol{v} \qquad \forall \boldsymbol{v} \in \mathbf{H}_\Gamma^1(\Omega),$$

$$\int_\Omega \rho_f J D_t \phi_f q + \int_\Omega \rho_f \phi_f J \mathbf{F}^{-1} \frac{\kappa(J, \phi_f)}{\mu_f} \mathbf{F}^{-t} \nabla p \cdot \nabla q$$

$$= \int_\Omega \rho_f J \ell(p, c_p) q \qquad \forall q \in H_\Sigma^1(\Omega),$$

$$\int_\Omega (J - \phi_f) \psi = \int_\Omega (1 - \phi_0) \psi \qquad \forall \psi \in L^2(\Omega). \tag{3.1}$$

We do not address time regularity in this work, and simply assume that the solution is weakly differentiable and continuous in time, the latter in order to obtain well-defined initial conditions. Next we partition the interval $[0, t_{\text{final}}]$ into N evenly spaced non-overlapping sub-intervals of fixed length Δt and apply a time semi-discretisation of (3.1) using the unconditionally stable, backward Euler's method. Starting from initial data, at each time iteration $n = 0, \ldots, N - 1$ we have a nonlinear problem with solution $(c_p^{n+1}, c_l^{n+1}) \in [H^1(\Omega)]^2$, $\boldsymbol{u}^{n+1} \in \mathbf{H}_\Gamma^1(\Omega)$, $p^{n+1} \in H_\Sigma^1(\Omega)$, and $\phi_f^{n+1} \in L^2(\Omega)$. Then we perform a Newton–Raphson method linearisation. This means that at each time step $n + 1$ we start the Newton iterates using as initial guess the solution at the previous time step $c_p^{k=0} = c_p^n$, $c_l^{k=0} = c_l^n$, $\boldsymbol{u}^{k=0} = \boldsymbol{u}^n$, $p^{k=0} = p^n$, $\phi_f^{k=0} = \phi_f^n$, and for $k = 0, 1, \ldots$ we look for the solution increments $(\delta c_p^{k+1}, \delta c_l^{k+1}) \in [H^1(\Omega)]^2$, $\delta \boldsymbol{u}^{k+1} \in \mathbf{H}_\Gamma^1(\Omega)$, $\delta p^{k+1} \in H_\Sigma^1(\Omega)$, $\delta \phi_f^{k+1} \in L^2(\Omega)$ satisfying

$$a_1(\delta c_p^{k+1}, w_p) + b_1^*(\delta c_l^{k+1}, w_p) + b_2^*(\delta \boldsymbol{u}^{k+1}, w_p) + b_3^*(\delta \phi_f^{k+1}, w_p)$$

$$= F_1(w_p) \qquad \forall w_p \in H^1(\Omega),$$

$$b_1(w_l, \delta c_p^{k+1}) + a_2(\delta c_l^{k+1}, w_l) + b_4^*(\delta \boldsymbol{u}^{k+1}, w_l) + b_5^*(\delta \phi_f^{k+1}, w_l)$$

$$= F_2(w_l) \qquad \forall w_l \in H^1(\Omega),$$

$$a_3(\delta \boldsymbol{u}^{k+1}, \boldsymbol{v}) + c_1^*(\delta p^{k+1}, \boldsymbol{v}) = F_3(\boldsymbol{v}) \qquad \forall \boldsymbol{v} \in \mathbf{H}_\Gamma^1(\Omega),$$

$$c_2(q, \delta c_p^{k+1}) + c_1(q, \delta \boldsymbol{u}^{k+1}) + a_4(\delta p^{k+1}, q) + c_3^*(\delta \phi_f^{k+1}, q) = F_4(q) \qquad \forall q \in H_\Sigma^1(\Omega),$$

$$c_4(\psi, \delta \boldsymbol{u}^{k+1}) - a_5(\delta \phi_f^{k+1}, \psi) = F_5(\psi) \qquad \forall \psi \in L^2(\Omega). \tag{3.2}$$

Then the solution is updated

$$c_p^{k+1} = c_p^k + \delta c_p^{k+1}, \quad c_l^{k+1} = c_l^k + \delta c_l^{k+1}, \quad \boldsymbol{u}^{k+1} = \boldsymbol{u}^k + \delta \boldsymbol{u}^{k+1},$$

$$p^{k+1} = p^k + \delta p^{k+1}, \quad \phi_f^{k+1} = \phi_f^k + \delta \phi_f^{k+1},$$

until either the increments or the residuals drop below a given tolerance. In order to specify these variational forms, as usual we use the directional derivatives of all nonlinearities at a particular trial solution in the direction of the increments. After rearranging terms and omitting the superscript $(\cdot)^{n+1}$ whenever clear from the context, the bilinear forms and linear functionals in (3.2) are defined as

$$a_1(\delta c_p, w_p) := \int_\Omega J^k \left(\frac{2\phi_f^k - \phi_f^n}{\Delta t} - \phi_f^k \frac{\partial r_p(c_p^k, c_l^k)}{\partial c_p^k} \right) \delta c_p w_p$$

$$+ \int_\Omega J^k \mathbf{F}^{k,-1} \mathbf{D}_p \mathbf{F}^{k,-\mathrm{t}} \nabla \delta c_p \cdot \nabla w_p,$$

$$b_1^*(\delta c_l, w_p) := - \int_\Omega J^k \frac{\partial r_p(\phi_f^k, c_p^k, c_l^k)}{\partial c_l^k} \delta c_l \, w_p, \quad F_1(w_p)$$

$$:= \int_\Omega \mathcal{R}_1^{k,n} w_p, \quad F_2(w_l) := \int_\Omega \mathcal{R}_2^{k,n} w_l,$$

$$b_2^*(\delta \boldsymbol{u}, w_p) := \int_\Omega J^k \mathbf{F}^{k,-1} \left([\mathbf{F}^{k,-\mathrm{t}} : \nabla \delta \boldsymbol{u}] \mathbf{D}_p - \nabla \delta \boldsymbol{u} \mathbf{F}^{k,-1} \mathbf{D}_p \right.$$

$$\left. - \mathbf{D}_p \mathbf{F}^{k,-\mathrm{t}} (\nabla \delta \boldsymbol{u})^{\mathrm{t}} \right) \mathbf{F}^{k,-\mathrm{t}} \nabla c_p^k \cdot \nabla w_p$$

$$+ \int_\Omega J^k \mathbf{F}^{k,-\mathrm{t}} : \nabla \delta \boldsymbol{u} \left(\frac{\phi_f^k - \phi_f^n}{\Delta t} c_p^k + \frac{c_p^k - c_p^n}{\Delta t} \phi_f^k - r_p(\phi_f^k, c_p^k, c_l^k) \right) w_p,$$

$$b_3^*(\delta \phi_f, w_p) := \int_\Omega J^k \left(\frac{2c_p^k - c_p^n}{\Delta t} - \frac{\partial r_p(\phi_f^k, c_p^k, c_l^k)}{\phi_f^k} \right) \delta \phi_f w_p,$$

$$F_3(w_l) := \int_\Omega \mathcal{R}_{3,\Omega}^k \cdot \boldsymbol{v} + \int_\Sigma \mathcal{R}_{3,\Sigma}^k \cdot \boldsymbol{v},$$

$$a_2(\delta c_l, w_l) := \int_\Omega J^k \left(\frac{2\phi_f^k - \phi_f^n}{\Delta t} - \frac{\partial r_l(\phi_f^k, c_p^k, c_l^k)}{\partial c_l^k} \right) \delta c_l w_l$$

$$+ \int_\Omega J^k \mathbf{F}^{k,-1} \mathbf{D}_l \mathbf{F}^{k,-\mathrm{t}} \nabla \delta c_l \cdot \nabla w_l$$

$$- \int_\Omega \chi J^k \delta c_l \mathbf{F}^{k,-1} \mathbf{F}^{k,-\mathrm{t}} \nabla c_p^k \cdot \nabla w_l,$$

$$b_1(w_l, \delta c_p) := - \int_\Omega \chi J^k c_l^k \mathbf{F}^{k,-1} \mathbf{F}^{k,-\mathrm{t}} \nabla \delta c_p \cdot \nabla w_l - \int_\Omega J^k \frac{\partial r_l(\phi_f^k, c_p^k, c_l^k)}{\partial c_p^k} \delta c_p w_l,$$

$$b_4^*(\delta \boldsymbol{u}, w_l) := \int_\Omega J^k \mathbf{F}^{k,-1} \left([\mathbf{F}^{k,-\mathrm{t}} : \nabla \delta \boldsymbol{u}] \mathbf{D}_l - \nabla \delta \boldsymbol{u} \mathbf{F}^{k,-1} \mathbf{D}_l \right.$$

$$\left. - \mathbf{D}_l \mathbf{F}^{k,-\mathrm{t}} (\nabla \delta \boldsymbol{u})^{\mathrm{t}} \right) \mathbf{F}^{k,-\mathrm{t}} \nabla c_l^k \cdot \nabla w_l$$

$$+ \int_\Omega J^k \mathbf{F}^{k,-\mathrm{t}} : \nabla \delta \boldsymbol{u} \left(\frac{\phi_f^k - \phi_f^n}{\Delta t} c_l^k + \frac{c_l^k - c_l^n}{\Delta t} \phi_f^k - r_l(\phi_f^k, c_p^k, c_l^k) \right) w_l$$

$$+ \int_\Omega \chi c_l^k J^k \left(\mathbf{F}^{k,-1} \nabla \delta \boldsymbol{u} \mathbf{F}^{k,-1} + \mathbf{F}^{k,-1} \mathbf{F}^{k,-\mathrm{t}} (\nabla \delta \boldsymbol{u})^{\mathrm{t}} - \mathbf{F}^{k,-\mathrm{t}} : \nabla \delta \boldsymbol{u} \mathbf{F}^{k,-1} \right)$$

$$\times \mathbf{F}^{k,-\mathrm{t}} \nabla c_p^k \cdot \nabla w_l,$$

$$b_5^*(\delta\phi_f, w_l) := \int_\Omega J^k \left(\frac{2c_l^k - c_l^n}{\Delta t} - \frac{\partial r_l(\phi_f^k, c_p^k, c_l^k)}{\phi_f^k} \right) \delta\phi_f w_l, \quad c_1^*(\delta p, \boldsymbol{v})$$

$$= -\int_\Omega \alpha \delta p J^k \mathbf{F}^{k,-\mathsf{t}} : \nabla \boldsymbol{v},$$

$$a_3(\delta\boldsymbol{u}, \boldsymbol{v}) := \int_\Omega \left(\frac{\partial \mathbf{P}_{\mathrm{eff}}(\mathbf{F}^k)}{\partial \mathbf{F}^k} \nabla \delta\boldsymbol{u} + \alpha p^k J^k [\mathbf{F}^{k,-\mathsf{t}} : \nabla \delta\boldsymbol{u}\, \mathbf{I} - \mathbf{F}^{k,-\mathsf{t}}(\nabla \delta\boldsymbol{u})^{\mathsf{t}}] \mathbf{F}^{k,-\mathsf{t}} \right) : \nabla \boldsymbol{v}$$

$$- \int_\Sigma J^k [\mathbf{F}^{k,-\mathsf{t}} : \nabla \delta\boldsymbol{u}\, \mathbf{I} - \mathbf{F}^{k,-\mathsf{t}}(\nabla \delta\boldsymbol{u})^{\mathsf{t}}] \mathbf{F}^{k,-\mathsf{t}} \boldsymbol{t}_\Sigma \cdot \boldsymbol{v},$$

$$c_1(q, \delta\boldsymbol{u}) := \int_\Omega \phi_f^k J^k \mathbf{F}^{k,-1} \left(\mathbf{F}^{k,-\mathsf{t}} : \nabla \delta\boldsymbol{u} \frac{\boldsymbol{\kappa}(J^k, \phi_f^k)}{\mu_f} \right.$$

$$\left. - \nabla \delta\boldsymbol{u} \mathbf{F}^{k,-1} \frac{\boldsymbol{\kappa}(J^k, \phi_f^k)}{\mu_f} - \frac{\boldsymbol{\kappa}(J^k, \phi_f^k)}{\mu_f} \mathbf{F}^{k,-\mathsf{t}}(\nabla \delta\boldsymbol{u})^{\mathsf{t}} \right)$$

$$\times \mathbf{F}^{k,-\mathsf{t}} \nabla p^k \cdot \nabla q + \int_\Omega \rho_f J^k \mathbf{F}^{k,-\mathsf{t}} : \nabla \delta\boldsymbol{u} \left(\frac{\phi_f^k - \phi_f^n}{\Delta t} - \ell(p^k, c_p^k) \right) q$$

$$a_4(\delta p, q) := \int_\Omega \phi_f^k J^k \mathbf{F}^{k,-1} \frac{\boldsymbol{\kappa}(J^k, \phi_f^k)}{\mu_f} \mathbf{F}^{k,-\mathsf{t}} \nabla \delta p \cdot \nabla q$$

$$- \int_\Omega \rho_f J^k \frac{\partial \ell(p^k, c_p^k)}{\partial p^k} \delta p\, q,$$

$$a_5(\delta\phi_f, \psi) := \int_\Omega \delta\phi_f \psi,$$

$$c_2(q, \delta c_p) := -\int_\Omega \rho_f J^k \frac{\partial \ell(p^k, c_p^k)}{\partial c_p^k} \delta c_p\, q, \quad F_4(q) := \int_\Omega \mathcal{R}_4^{k,n} q, \quad F_5(\psi) := \int_\Omega \mathcal{R}_5^k \psi,$$

$$c_3^*(\delta\phi_f, q) := \int_\Omega \frac{J^k}{\mu_f} \mathbf{F}^{k,-1} \frac{\partial [\boldsymbol{\kappa}(J^k, \phi_f^k) \cdot \phi_f^k]}{\partial \phi_f^k} \delta\phi_f \mathbf{F}^{k,-\mathsf{t}} \nabla p^k \cdot \nabla q + \int_\Omega \rho_f J^k \frac{\delta\phi_f}{\Delta t} q,$$

$$c_4(\psi, \delta\boldsymbol{u}) := \int_\Omega J^k \mathbf{F}^{k,-\mathsf{t}} : \nabla \delta\boldsymbol{u}\, \psi, \tag{3.3}$$

where $\mathbf{F}^k = \mathbf{I} + \nabla \boldsymbol{u}^k$, $J^k = \det \mathbf{F}^k$, $\mathbf{F}^{k,-1} = (\mathbf{F}^k)^{-1}$, $\mathbf{F}^{k,-\mathsf{t}} = (\mathbf{F}^k)^{-\mathsf{t}}$, and $\mathcal{R}_{3,\Omega}^k, \mathcal{R}_{3,\Sigma}^k, \mathcal{R}_5^k$ are vector and scalar residuals coming from the linearisation of (2.2a) and (2.2c) and containing terms associated with the previous Newton step k as well as body and traction loads. The terms $\mathcal{R}_1^{k,n}, \mathcal{R}_2^{k,n}, \mathcal{R}_4^{k,4}$ are scalar residuals from the linearisation of (2.4a), (2.4b), and (2.2b), respectively; which in addition contain contributions from the previous time step n.

4 Stability and Solvability of the Linearised Problem

4.1 Definition and Preliminaries

For this section we draw inspiration from the stability analysis of a system similar to (2.2), recently proved in [12]; and from the study of the linearised hyperelasticity equations, recently studied in [36]. We restrict the description to neo–Hookean poroelastic solids with material parameters μ_s, λ_s, for which the effective first Piola–Kirchhoff stress tensor is

$$\mathbf{P}_{\text{eff}} = \mu_s (\mathbf{F} - \mathbf{F}^{-\text{t}}) + \lambda_s \ln(J) \, \mathbf{F}^{-\text{t}}.$$

Note that a simplified version of the time-discrete tangent system (3.2) is readily obtained by focusing on the first Newton–Raphson iterate when starting from the following initial guess

$$\boldsymbol{u}^k = \mathbf{0}, \quad p^k = p_0, \quad \phi_f^k = \phi_0, \quad c_p^k = c_l^k = 0,$$

for displacement, fluid pressure, nominal porosity and species concentrations, which gives $D_t \phi_f^k = 0$, $\mathbf{F}^k = \mathbf{I}$, $J^k = 1$, $\nabla p^k = \mathbf{0}$. In addition, the residuals can be conveniently rearranged and we rescale the system in an appropriate manner using the parameters ρ_f, Δt, α, μ_s, ϕ_0, and λ_s. Next we introduce the total pressure

$$\zeta := \alpha p - \lambda_s \operatorname{div} \boldsymbol{u}, \tag{4.1}$$

and the system can be recast in terms of $\boldsymbol{u}, \zeta, p, c_p, c_l$ (that is, using ζ instead of ϕ_f), as follows

$$\tilde{a}_1(c_p, w_p) + a_1(c_p, w_p) + \beta_1 b_3^*(p, w_p) + \beta_2 b_3^*(\zeta, w_p) = \tilde{F}_1(w_p) \qquad \forall w_p \in \mathrm{H}^1(\Omega),$$

$$\tilde{a}_2(c_l, w_l) + a_2(c_l, w_l) + \beta_1 b_5^*(p, w_l) + \beta_2 b_5^*(\zeta, w_l) = \tilde{F}_2(w_l) \qquad \forall w_l \in \mathrm{H}^1(\Omega),$$

$$a_3(\boldsymbol{u}, \boldsymbol{v}) + b_1(\zeta, \boldsymbol{v}) = F_3(\boldsymbol{v}) \qquad \forall \boldsymbol{v} \in \mathbf{H}_\Gamma^1(\Omega),$$

$$b_4(c_p, q) \, \tilde{a}_4(p, q) + a_4(p, q) - \frac{1}{\alpha} b_2(\delta_t \zeta, q) = \tilde{F}_4(q) \qquad \forall q \in \mathrm{H}_\Sigma^1(\Omega),$$

$$b_1(\psi, \boldsymbol{u}) + b_2(\psi, p) - a_5(\zeta, \psi) = 0 \qquad \forall \psi \in \mathrm{L}^2(\Omega), \tag{4.2}$$

where for a function scalar X^{n+1}, the expression $\delta_t X^{n+1}$ stands for $\frac{X^{n+1} - X^n}{\Delta t}$, and where we have renamed the bilinear forms, which are now defined as

$$\tilde{a}_1(c_p, w_p) = \int_\Omega \delta_t c_p w_p, \quad a_1(c_p, w_p) = \int_\Omega \mathbf{D}_p \nabla c_p \cdot \nabla w_p,$$

$$b_1(\psi, \boldsymbol{v}) = -\int_\Omega \operatorname{div} \boldsymbol{v} \, \psi, \quad b_3^*(\zeta, w_p) = -\frac{1}{\Delta t} \int_\Omega \zeta w_p,$$

$$\tilde{a}_2(c_l, w_l) = \int_\Omega \delta_t c_l w_l, \quad a_2(c_l, w_l) = \int_\Omega \mathbf{D}_l \nabla c_l \cdot \nabla w_l,$$

$$a_5(\zeta, \psi) = \frac{1}{\lambda_s} \int_\Omega \zeta \psi, \quad \tilde{F}_4(q) = \int_\Omega \left(\frac{1}{\Delta t} \tilde{R}_4^n - R_4 \right) q,$$

$$b_5^*(\zeta, w_l) = -\frac{1}{\Delta t} \int_\Omega \zeta w_l, \quad b_2(\psi, q) = \frac{\alpha}{\lambda_s} \int_\Omega q \psi,$$

$$b_4(w_p, q) = \frac{-1}{\Delta t} \int_\Omega w_p q, \quad a_3(\boldsymbol{u}, \boldsymbol{v}) = 2\mu_s \int_\Omega \boldsymbol{\epsilon}(\boldsymbol{u}) : \boldsymbol{\epsilon}(\boldsymbol{v}),$$

$$\tilde{a}_4(p, q) = \left(1 + \frac{\alpha}{\lambda_s}\right) \int_\Omega \delta_t p q, \quad a_4(p, q) = \int_\Omega \frac{\kappa}{\mu_f} \nabla p \cdot \nabla q,$$

$$c_3^*(\zeta, q) = -\frac{\rho_f}{\Delta t} \int_\Omega \zeta q, \quad F_3(\boldsymbol{v}) = \int_\Omega (\rho_s \boldsymbol{b} + \mathbf{R}_3) \cdot \boldsymbol{v},$$

$$\tilde{F}_1(w_p) = \int_\Omega \left(\frac{1}{\Delta t} \tilde{R}_1^n + R_1 \right) w_p, \quad \tilde{F}_2(w_l) = \int_\Omega \left(\frac{1}{\Delta t} \tilde{R}_2^n + R_2 \right) w_l. \quad (4.3)$$

Here we have also set $\boldsymbol{t}_\Sigma = \boldsymbol{0}$. Note that the linear variational problem (4.2) corresponds to the linear and coupled reaction-diffusion / three-field Biot equations

$$\delta_t c_p - \frac{1}{\Delta t}(\beta_1 p + \beta_2 \zeta) - \operatorname{div}(\mathbf{D}_p \nabla c_p) = \frac{1}{\Delta t} \tilde{R}_1^n + R_1,$$

$$\delta_t c_l - \frac{1}{\Delta t}(\beta_1 p + \beta_2 \zeta) - \operatorname{div}(\mathbf{D}_l \nabla c_l) = \frac{1}{\Delta t} \tilde{R}_2^n + R_2,$$

$$-\operatorname{\mathbf{div}}(2\mu_s \boldsymbol{\epsilon}(\boldsymbol{u}) - \zeta \mathbf{I}) = \rho_s \boldsymbol{b} + \mathbf{R}_3,$$

$$-\frac{1}{\Delta t} c_p + \left(1 + \frac{\alpha}{\lambda_s}\right)\delta_t p - \frac{1}{\lambda_s}\delta_t \zeta - \operatorname{div}\left(\frac{\kappa}{\mu_f}\nabla p\right) = \frac{1}{\Delta t} \tilde{R}_4^n - R_4,$$

$$\frac{\alpha}{\lambda_s} p - \frac{1}{\lambda_s}\zeta - \operatorname{div}\boldsymbol{u} = 0, \quad (4.4)$$

where the R_i's and $\tilde{R}_i$'s are scalar and vector residuals, and the $\beta_i > 0$ are additional constants arising from the linearisation of the reaction terms and from the change of variables (4.1). A variant of system (4.4) including advection and nonlinear reaction, has been studied in [77]. We follow that reference and in the remainder of this section we present the solvability, stability, and convergence analysis for the in-time problem associated with (4.2).

We will assume that the anisotropic permeability κ and the diffusion matrices D_p, D_l are uniformly bounded and positive definite in Ω. The latter means that, there exist positive constants κ_1, κ_2, and $D_i^{\min}$, $D_i^{\max}$, $i \in \{p, l\}$, such that

$$\kappa_1 |\boldsymbol{w}|^2 \leq \boldsymbol{w}^{\mathrm{t}} \kappa \boldsymbol{w} \leq \kappa_2 |\boldsymbol{w}|^2, \quad \text{and} \quad D_i^{\min}|\boldsymbol{w}|^2 \leq \boldsymbol{w}^{\mathrm{t}} D_i \boldsymbol{w} \leq D_i^{\max}|\boldsymbol{w}|^2 \quad \forall \boldsymbol{w} \in \mathbb{R}^d.$$

We also recall the following version of Korn's inequality, valid for all $\boldsymbol{u} \in \mathbf{H}_\Gamma^1(\Omega)$

$$C_{k,1}\|\boldsymbol{u}\|_{1,\Omega}^2 \leq \|\boldsymbol{\varepsilon}(\boldsymbol{u})\|_{0,\Omega}^2,$$

where $C_{k,1}$ is a positive constant (see, e.g., [20]). This bound, together with the assumptions above on the permeability and diffusivity, imply the following coercivity and positivity properties

$$a_1(w_p, w_p) \geq D_p^{\min}|w_p|_{1,\Omega}^2, \quad a_2(w_l, w_l) \geq D_l^{\min}|w_l|_{1,\Omega}^2,$$

$$a_3(\boldsymbol{v}, \boldsymbol{v}) \geq 2\mu_s C_{k,1}\|\boldsymbol{v}\|_{1,\Omega}^2, \quad a_4(q, q) \geq \frac{\kappa_1}{\mu_f}\|q^f\|_{1,\Omega}^2, \quad a_5(\zeta, \zeta) = \lambda_s^{-1}\|\zeta\|_{0,\Omega}^2,$$

$$(4.5)$$

for all $\boldsymbol{v} \in \mathbf{H}_\Gamma^1(\Omega)$, $\zeta \in \mathrm{L}^2(\Omega)$, $w_p, w_l \in \mathrm{H}^1(\Omega)$, $q \in \mathrm{H}_\Sigma^1(\Omega)$. Moreover, thanks to the structure of the formulation, the bilinear form b_1 (which coincides with the usual non-diagonal bilinear form in the Stokes equations) satisfies the following inf-sup condition (see, e.g., [44]): For every $\zeta \in \mathrm{L}^2(\Omega)$, there exists $\beta > 0$ such that

$$\sup_{\boldsymbol{v} \in \mathbf{H}_\Gamma^1(\Omega)} \frac{b_1(\boldsymbol{v}, \zeta)}{\|\boldsymbol{v}\|_{1,\Omega}} \geq \beta \|\zeta\|_{0,\Omega}. \quad (4.6)$$

Finally, we recall an important discrete-in-time identity and introduce the discrete-in-time norm

$$\int_\Omega X^{n+1} \delta_t X^{n+1} = \frac{1}{2}\delta_t \|X^{n+1}\|^2 + \frac{1}{2}\Delta t \|\delta_t X^{n+1}\|^2, \qquad \|X\|^2_{\ell^2(V)} := \Delta t \sum_{m=0}^{n} \|X^{m+1}\|^2_V,$$

respectively, which will be useful for the subsequent analysis.

4.2 Fixed-point Scheme and Unique Solvability of the Decoupled Problems

With the aim to facilitate the comprehension and clarity of the forthcoming analysis, through this section and Sects. 4.3–4.5, we take up again the notation $(\cdot)^{n+1}$ given in Sect. 3.1 to denote the current time step of the involved variables. Moreover, in order to apply a fixed-point scheme, we modify the variational formulation (4.2) in an equivalent one: find $(c_p^{n+1}, c_l^{n+1}, \boldsymbol{u}^{n+1}, p^{n+1}, \zeta^{n+1}) \in H^1(\Omega) \times H^1(\Omega) \times \mathbf{H}_\Gamma^1(\Omega) \times H_\Sigma^1(\Omega) \times L^2(\Omega)$ such that

$$\tilde{a}_1(c_p^{n+1}, w_p) + a_1(c_p^{n+1}, w_p) = F_{1,p^{n+1},\zeta^{n+1}}(w_p), \qquad (4.7a)$$

$$\tilde{a}_2(c_l^{n+1}, w_l) + a_2(c_l^{n+1}, w_l) = F_{2,p^{n+1},\zeta^{n+1}}(w_l), \qquad (4.7b)$$

$$a_3(\boldsymbol{u}^{n+1}, \boldsymbol{v}) + b_1(\zeta^{n+1}, \boldsymbol{v}) = F_3(\boldsymbol{v}), \qquad (4.7c)$$

$$\tilde{a}_4(p^{n+1}, q) + a_4(p^{n+1}, q) - \frac{1}{\alpha}b_2(\delta_t \zeta^{n+1}, q) = F_{4,c_p^{n+1}}(q), \qquad (4.7d)$$

$$b_1(\psi, \boldsymbol{u}^{n+1}) + b_2(\psi, p^{n+1}) - a_5(\zeta^{n+1}, \psi) = 0, \qquad (4.7e)$$

for each $(w_p, w_l, \boldsymbol{v}, q, \psi) \in H^1(\Omega) \times H^1(\Omega) \times \mathbf{H}_\Gamma^1(\Omega) \times H_\Sigma^1(\Omega) \times L^2(\Omega)$, where the functionals $F_{1,p^{n+1},\zeta^{n+1}}$, $F_{2,p^{n+1},\zeta^{n+1}}$, $F_{4,c_p^{n+1}}$ are defined as

$$F_{1,q,\psi}(w_p) := \tilde{F}_1(w_p) - \beta_1 b_3^*(q, w_p) - \beta_2 b_3^*(\psi, w_p),$$
$$F_{2,q,\psi}(w_l) := \tilde{F}_2(w_l) - \beta_1 b_3^*(q, w_l) - \beta_2 b_3^*(\psi, w_l),$$
$$F_{4,w_p}(q) := \tilde{F}_4(q) - b_4(w_p, q), \qquad (4.8)$$

respectively.

We then start with the fixed-point strategy. Let us define the operator $\mathbf{S} : H^1(\Omega) \to H_\Sigma^1(\Omega) \times L^2(\Omega)$ as

$$\mathbf{S}(c_p^{n+1}) := (\mathbf{S}_1(c_p^{n+1}), \mathbf{S}_2(c_p^{n+1})) := (p^{n+1}, \zeta^{n+1}) \quad \forall c_p^{n+1} \in H^1(\Omega), \qquad (4.9)$$

where $p^{n+1} \in H_\Sigma^1(\Omega)$ and $\zeta^{n+1} \in L^2(\Omega)$ are the second and third components of the solution of problem: Find $(\boldsymbol{u}^{n+1}, p^{n+1}, \zeta^{n+1}) \in \mathbf{H}_\Gamma^1(\Omega) \times H_\Sigma^1(\Omega) \times L^2(\Omega)$ such that

$$a_3(\boldsymbol{u}^{n+1}, \boldsymbol{v}) + b_1(\zeta^{n+1}, \boldsymbol{v}) = F_3(\boldsymbol{v}) \qquad \forall \boldsymbol{v} \in \mathbf{H}_\Gamma^1(\Omega), \qquad (4.10a)$$

$$\tilde{a}_4(p^{n+1}, q) + a_4(p^{n+1}, q) - \frac{1}{\alpha}b_2(\delta_t \zeta^{n+1}, q) = F_{4,c_p^{n+1}}(q) \qquad \forall q \in H_\Sigma^1(\Omega), \qquad (4.10b)$$

$$b_1(\psi, \boldsymbol{u}^{n+1}) + b_2(\psi, p^{n+1}) - a_5(\zeta^{n+1}, \psi) = 0 \qquad \forall \psi \in L^2(\Omega), \qquad (4.10c)$$

for a given $c_p^{n+1} \in H^1(\Omega)$. In turn, let $\tilde{\mathbf{S}} : H_\Sigma^1(\Omega) \times L^2(\Omega) \to H^1(\Omega)$ be the operator defined by

$$\tilde{\mathbf{S}}(p^{n+1}, \zeta^{n+1}) := c_p^{n+1} \quad \forall (p^{n+1}, \zeta^{n+1}) \in H_\Sigma^1(\Omega) \times L^2(\Omega), \qquad (4.11)$$

where $c_p^{n+1} \in H^1(\Omega)$ is the first component of the solution of the problem: Find $(c_p^{n+1}, c_l^{n+1}) \in [H^1(\Omega)]^2$ such that

$$\tilde{a}_1(c_p^{n+1}, w_p) + a_1(c_p^{n+1}, w_p) = F_{1, p^{n+1}, \zeta^{n+1}}(w_p) \qquad \forall w_p \in H^1(\Omega), \qquad (4.12a)$$

$$\tilde{a}_2(c_l^{n+1}, w_l) + a_2(c_l^{n+1}, w_l) = F_{2, p^{n+1}, \zeta^{n+1}}(w_l) \qquad \forall w_l \in H^1(\Omega), \qquad (4.12b)$$

for a given pair $(p^{n+1}, \zeta^{n+1}) \in H_\Sigma^1(\Omega) \times L^2(\Omega)$. Therefore, we define the map $\mathbf{T} : H^1(\Omega) \to H^1(\Omega)$ as

$$\mathbf{T}(c_p^{n+1}) := \tilde{\mathbf{S}}(\mathbf{S}_1(c_p^{n+1}), \mathbf{S}_2(c_p^{n+1})) \quad \forall c_p^{n+1} \in H^1(\Omega), \qquad (4.13)$$

and one readily realises that solving (4.7a)–(4.7e) is equivalent to seeking a fixed point of the solution operator $\mathbf{T}$.

Now, in order to prove that the operator $\mathbf{T}$ is well-defined, we first need to investigate whether the uncoupled problems defined by the operators $\mathbf{S}$ and $\tilde{\mathbf{S}}$ are well-posed. The fact that the poroelastic problem is well-posed for a given c_p^{n+1} is given next. Its proof can be deduced by employing the Fredholm alternative approach and classical tools frequently used for showing the well-posedness of elliptic/parabolic equations. We refer to [77, Lemmas 2.1, 2.2 and 2.3] for further details.

Lemma 4.1 *For a given $c_p^{n+1} \in H^1(\Omega)$, the problem (4.10a)–(4.10c) has a unique solution $(\boldsymbol{u}^{n+1}, p^{n+1}, \zeta^{n+1}) \in \mathbf{H}_\Gamma^1(\Omega) \times H_\Sigma^1(\Omega) \times L^2(\Omega)$. Moreover, there exists $C > 0$, independent of λ_s, such that for each n,*

$$\|\boldsymbol{u}^{n+1}\|_{1,\Omega}^2 + \|p^{n+1}\|_{0,\Omega}^2 + \|\zeta^{n+1}\|_{0,\Omega}^2 + \|p\|_{\ell^2(H^1(\Omega))}^2$$

$$\leq \exp(C) \left\{ \|\boldsymbol{u}^0\|_{1,\Omega}^2 + \|p^0\|_{0,\Omega}^2 + \|\zeta^0\|_{0,\Omega}^2 + \|\mathbf{R}_3\|_{0,\Omega}^2 + \|\boldsymbol{b}\|_{0,\Omega}^2 + \Delta t \|R_4\|_{0,\Omega}^2 \right.$$

$$\left. + \sum_{m=0}^{n} \|\tilde{R}_4^m\|_{0,\Omega}^2 + \sum_{m=0}^{n} \|c_p^{m+1}\|_{0,\Omega}^2 \right\}. \qquad (4.14)$$

In turn, the well-posedness of the uncoupled diffusion-reaction problem is given next.

Lemma 4.2 *For fixed $p^{n+1} \in H_\Sigma^1(\Omega)$ and $\zeta^{n+1} \in L^2(\Omega)$, the system of nonlinear parabolic Eqs. (4.12a)–(4.12b) has a unique solution $(c_p^{n+1}, c_l^{n+1}) \in [H^1(\Omega)]^2$, that is continuously dependent on data, that is, there exists $C > 0$, such that for each n,*

$$\|c_p^{n+1}\|_{0,\Omega}^2 + \|c_l^{n+1}\|_{0,\Omega}^2 + \|\nabla c_p\|_{\ell^2(L^2(\Omega))}^2 + \|\nabla c_l\|_{\ell^2(L^2(\Omega))}^2$$

$$\leq \exp(C) \left\{ \|c_p^0\|_{0,\Omega}^2 + \|c_l^0\|_{0,\Omega}^2 + \sum_{m=0}^{n} (\|\tilde{R}_1^m\|_{0,\Omega}^2 + \|\tilde{R}_2^m\|_{0,\Omega}^2) \right.$$

$$+ \Delta t \|R_1\|_{0,\Omega}^2 + \Delta t \|R_2\|_{0,\Omega}^2$$

$$\left. + \sum_{m=0}^{n} (\|\zeta^{m+1}\|_{0,\Omega}^2 + \|p^{m+1}\|_{0,\Omega}^2) \right\}. \qquad (4.15)$$

Proof For each n, the unique solvability of (4.12a)–(4.12b) can be obtained by using the coercivity of the diffusivities $\mathbf{D}_i \ i \in \{p, l\}$, and classical tools for time-discrete approximation schemes of parabolic equations (see for instance [64]). Regarding stability, we focus first on the equation for c_p^{n+1}. Consider $w_p = c_p^{n+1}$ in (4.12a), to get

$$\int_\Omega \delta_t c_p^{n+1} c_p^{n+1} + \int_\Omega \mathbf{D}_p \nabla c_p^{n+1} \cdot \nabla c_p^{n+1} = \int_\Omega \left(\frac{1}{\Delta t} \tilde{R}_1^n + R_1 \right) c_p^{n+1} + \beta_1 \frac{1}{\Delta t} \int_\Omega \zeta^{n+1} c_p^{n+1}$$

$$+\beta_2 \frac{1}{\Delta t} \int_\Omega p^{n+1} c_p^{n+1},$$

and then, applying the property (4.5), and the classical Cauchy–Schwarz inequality, we obtain

$$\frac{1}{2}\delta_t \|c_p^{n+1}\|_{0,\Omega}^2 + \frac{1}{2}\Delta t \|\delta_t c_p^{n+1}\|_{0,\Omega}^2 + D_p^{\min}\|\nabla c_p^{n+1}\|_{0,\Omega}^2$$

$$\leq \frac{1}{\Delta t}\|\tilde{R}_1^n\|_{0,\Omega}\|c_p^{n+1}\|_{0,\Omega} + \|R_1\|_{0,\Omega}\|c_p^{n+1}\|_{0,\Omega}$$

$$+ \frac{1}{\Delta t}\|\beta_1 \zeta^{n+1} + \beta_2 p^{n+1}\|_{0,\Omega}\|c_p^{n+1}\|_{0,\Omega}.$$

Applying Young's inequality, it is possible to get

$$\frac{1}{2}\delta_t \|c_p^{n+1}\|_{0,\Omega}^2 + \frac{1}{2}\Delta t \|\delta_t c_p^{n+1}\|_{0,\Omega}^2 + D_p^{\min}\|\nabla c_p^{n+1}\|_{0,\Omega}^2$$

$$\leq \frac{1}{2\Delta t}\|\tilde{R}_1^n\|_{0,\Omega}^2 + \left(\frac{1}{\Delta t} + \frac{1}{2}\right)\|c_p^{n+1}\|_{0,\Omega}^2 + \frac{1}{2}\|R_1\|_{0,\Omega}^2$$

$$+ \frac{\beta_1}{2\Delta t}\|\zeta^{n+1}\|_{0,\Omega}^2 + \frac{\beta_2}{2\Delta t}\|p^{n+1}\|_{0,\Omega}^2,$$

and summing over $n-1$ and multiplying by Δt, we finally deduce that

$$\frac{1}{2}\|c_p^n\|_{0,\Omega}^2 + \frac{1}{2}\Delta t^2 \sum_{m=0}^{n-1} \|\delta_t c_p^{m+1}\|_{0,\Omega}^2 + D_p^{\min}\Delta t \sum_{m=0}^{n-1}\|\nabla c_p^{m+1}\|_{0,\Omega}^2$$

$$\leq \|c_p^0\|_{0,\Omega}^2 + \frac{1}{2}\sum_{m=0}^{n-1}\|\tilde{R}_1^m\|_{0,\Omega}^2 + (1+\frac{\Delta t}{2})\sum_{m=0}^{n-1}\|c_p^{m+1}\|_{0,\Omega}^2 + \frac{\Delta t}{2}\sum_{m=0}^{n-1}\|R_1\|_{0,\Omega}^2 \quad (4.16)$$

$$+ \frac{\beta_1}{2}\sum_{m=0}^{n-1}\|\zeta^{m+1}\|_{0,\Omega}^2 + \frac{\beta_2}{2}\sum_{m=0}^{n-1}\|p^{m+1}\|_{0,\Omega}^2.$$

The same result can be derived for c_l^n. Finally, the estimate (4.15) follows by adding the aforementioned result to (4.16) and then, applying Gronwall's inequality, and using the resulting approach for $n+1$. □

4.3 Existence of a Weak Solution to the Coupled Linearised System

Let us define a closed subset of the Banach space $L^2(\Omega)$ as

$$\mathcal{K} := \{c_p^{n+1} \in L^2(\Omega): \quad \|c_p^{n+1}\|_{1,\Omega} \leq r\}, \quad (4.17)$$

for a given $r > 0$. We then restrict the space in (4.13) to the ball (4.17), and therefore, we look for a $c_p^{n+1} \in \mathcal{K}$ such that $\mathbf{T}(c_p^{n+1}) = c_p^{n+1}$. In what follows, we prove the existence of that c_p^{n+1} by means of the Schauder fixed-point approach. We start with a preliminary result.

Lemma 4.3 *For a given $c_p^{n+1} \in H^1(\Omega)$, the problem defined by the operator $\mathbf{S}$ (cf. (4.9)) satisfies the following estimate*

$$\|\mathbf{S}(c_p^{n+1})\|_{0,\boldsymbol{\Omega}} \leq \|p^{n+1}\|_{1,\Omega} + \|\zeta^{n+1}\|_{0,\Omega}$$

$$\leq C\Big\{\|\mathbf{R}_3\|_{0,\Omega} + \|\boldsymbol{b}^{m+1}\|_{0,\Omega} + \|R_4\|_{0,\Omega} + \|\tilde{R}_4^n\|_{0,\Omega} + \|\zeta^n\|_{0,\Omega}\Big\} + \tilde{C}\|c_p^{n+1}\|_{0,\Omega}, \quad (4.18)$$

where C and $\tilde{C}$ are positive constants depending on Δt, μ_f, μ_s, κ_1, β, α, with

$$\tilde{C} := (3\alpha\mu_f((2\Delta t^2\kappa_1)\min\{\mu_s/\Delta t, \alpha\kappa_1/2\mu_f, \beta^2\})^{-1})^{1/2}. \tag{4.19}$$

Proof The proof starts by multiplying the Eqs. (4.10a), (4.10b) and (4.10c) by $\frac{1}{\Delta t}$, α, and $-\frac{1}{\Delta t}$, respectively. Then, the estimate (4.18) follows after adding these resulting equations with $v := u^{n+1}$, $q := p^{n+1}$ and $\psi := \zeta^{n+1}$, respectively, using Cauchy–Schwarz and Young inequalities. We omit further details.   □

Now, we are in a position to establish the existence of a fixed point of the operator **T**. This result is abridged in the following two lemmas.

Lemma 4.4 *Assume that $\tilde{C}\hat{C} \leq \frac{1}{4}$, and*

$$\hat{C}\left\{\|c_p^n\|_{0,\Omega} + \|\tilde{R}_1^n\|_{0,\Omega} + \|R_1\|_{0,\Omega}\right.$$
$$\left. +C\left\{\|\mathbf{R}_3\|_{0,\Omega} + \|b^{m+1}\|_{0,\Omega} + \|R_4\|_{0,\Omega} + \|\tilde{R}_4^n\|_{0,\Omega} + \|\zeta^n\|_{0,\Omega}\right\}\right\} \leq \frac{r}{2},$$

where $\tilde{C}$, $\hat{C}$ and C are the constants specified in (4.19), (4.22) and (4.18), respectively. Then, the fixed-point operator **T** *maps from $\mathcal{K}$ into itself.*

Proof We begin by obtaining an energy estimate for the problem defined by $\tilde{\mathbf{S}}$ (cf. (4.11)). In fact, by taking $w_p = c_p^{n+1}$ in (4.12a), we readily see that

$$\frac{1}{\Delta t}\|c_p^{n+1}\|_{0,\Omega}^2 + \mathbf{D}_p^{min}\|\nabla c_p^{n+1}\|_{0,\Omega}^2$$
$$\leq \frac{1}{\Delta t}\int_\Omega c_p^{n+1}c_p^n + \int_\Omega (\frac{1}{\Delta t}\tilde{R}_1^n + R_1)c_p^{n+1}$$
$$+ \beta_1\frac{1}{\Delta t}\int_\Omega \zeta^{n+1}c_p^{n+1} + \beta_2\frac{1}{\Delta t}\int_\Omega p^{n+1}c_p^{n+1},$$

for a given pair $(p^{n+1}, \zeta^{n+1}) \in H_\Sigma^1(\Omega) \times L^2(\Omega)$, from which, we straightforwardly obtain

$$\|\tilde{\mathbf{S}}(p^{n+1}, \zeta^{n+1})\|_{1,\Omega} = \|c_p^{n+1}\|_{1,\Omega}$$
$$\leq \hat{C}\left\{\|c_p^n\|_{0,\Omega} + \|\tilde{R}_1^n\|_{0,\Omega} + \|R_1\|_{0,\Omega} + \|p^{n+1}\|_{0,\Omega} + \|\zeta^{n+1}\|_{0,\Omega}\right\}, \tag{4.20}$$

and therefore, by using the definition of **T** (cf. (4.13)), and applying the result given by (4.20), we get

$$\|\mathbf{T}(c_p^{n+1})\|_{1,\Omega} := \|\tilde{\mathbf{S}}(\mathbf{S}_1(c_p^{n+1}), \mathbf{S}_2(c_p^{n+1}))\|_{1,\Omega}$$
$$\leq \hat{C}\left\{\|c_p^n\|_{0,\Omega} + \|\tilde{R}_1^n\|_{0,\Omega} + \|R_1\|_{0,\Omega}\right. \tag{4.21}$$
$$\left. +\|\mathbf{S}_1(c_p^{n+1})\|_{0,\Omega} + \|\mathbf{S}_2(c_p^{n+1})\|_{0,\Omega}\right\},$$

where

$$\hat{C} := (\Delta t)^{-1}\max\{1, (\Delta t)^{-1}, \beta_1, \beta_2\} \cdot \min\{(\Delta t)^{-1}, D_p^{min}\}^{-1}. \tag{4.22}$$

Finally, the desired result follows after substituting the estimate (4.18) into (4.21), and then, applying the assumption on data given at the statement of the present lemma.   □

We remark that there is no inconvenience with the second assumption on data given in Lemma 4.4 since it depends on a constant r that can be appropriately chosen (cf. (4.17)). Moreover, the first smallness assumption given in Lemma 4.4 is merely a theoretical condition to guarantee solvability of the continuous problem. However, even though for the constants $\tilde{C}$ and $\hat{C}$ defined by (4.19) and (4.22), respectively, the condition might not always be satisfied (especially for extreme values of the model constants), the numerical experiments obtained in Sect. 6 show satisfactory results even even without verifying the theoretical constraints. The present analysis could be improved by using a different approach that circumvents the current restrictions on data, but we are not aware of such a strategy being applicable directly to this context.

Lemma 4.5 *The map* $\mathbf{T} : \mathcal{K} \to \mathcal{K}$ *is continuous and* $\mathbf{T}(\mathcal{K})$ *is relatively compact in* $\mathrm{L}^2(\Omega)$.

Proof We notice from the previous lemma, that $\mathbf{T}(\mathcal{K})$ is bounded in $\mathrm{H}^1(\Omega)$. In this way, the compact embedding of $\mathrm{H}^1(\Omega)$ into $\mathrm{L}^2(\Omega)$ together with boundedness of $\mathbf{T}(\mathcal{K})$ conclude that $\mathbf{T}(\mathcal{K})$ is relatively compact in $\mathrm{L}^2(\Omega)$. On the other hand, for the continuity property, we let $\{c_{p,k}^{n+1}\}_k \in \mathcal{K}$ be a sequence such that $c_{p,k}^{n+1} \to c_p^{n+1}$ in $\mathrm{L}^2(\Omega)$ as $k \to \infty$, and as is known from (4.13), $c_{p,k}^{n+1} = \mathbf{T}(c_{p,k}^{n+1})$. In this way, proceeding as in [77, Lemma 2.8], we obtain that $c_{p,k}^{n+1} \to \mathbf{T}(c_p^{n+1})$ in $\mathrm{L}^2(\Omega)$ as $k \to \infty$, concluding the proof. $\square$

Finally, the following lemma concerning the existence of solution for problem (4.7a)–(4.7e), is merely an application of Lemmas 4.4 and 4.5, and the Schauder fixed-point theorem.

Lemma 4.6 *The semi-discrete in-time formulation* (4.7a)–(4.7e) *possesses at least one solution.*

4.4 Uniqueness of Weak Solutions

We establish the uniqueness of weak solutions through the following result.

Lemma 4.7 *The semi-discrete weak formulation* (4.7a)–(4.7e) *has a unique solution.*

Proof We begin by defining two solutions $(\boldsymbol{u}_1^{n+1}, p_1^{n+1}, \zeta_1^{n+1}, c_{p,1}^{n+1}, c_{l,1}^{n+1})$ and $(\boldsymbol{u}_2^{n+1}, p_2^{n+1}, \zeta_2^{n+1}, c_{p,2}^{n+1}, c_{l,2}^{n+1})$ associated with initial data $\boldsymbol{b}_1, \boldsymbol{u}_1^0, p_1^0, \zeta_1^0, c_{p,1}^0, c_{l,1}^0, R_{1,1}, \tilde{R}_{1,1}^n, R_{2,1}, \tilde{R}_{2,1}^n, \mathbf{R}_{3,1}, R_{4,1}, \tilde{R}_{4,1}^n$ and $\boldsymbol{b}_2, \boldsymbol{u}_2^0, p_2^0, \zeta_2^0, c_{p,2}^0, c_{l,2}^0, R_{1,2}, \tilde{R}_{1,2}^n, R_{2,2}, \tilde{R}_{2,2}^n, \mathbf{R}_{3,2}, R_{4,2}, \tilde{R}_{4,2}$, respectively, and then

$$\mathcal{U}^{n+1} = \boldsymbol{u}_1^{n+1} - \boldsymbol{u}_2^{n+1}, \quad \mathcal{P}^{n+1} = p_1^{n+1} - p_2^{n+1}, \quad \chi^{n+1} = \zeta_1^{n+1} - \zeta_2^{n+1},$$
$$\mathcal{C}_p^{n+1} = c_{p,1}^{n+1} - c_{p,2}^{n+1}, \quad \mathcal{C}_l^{n+1} = c_{l,1}^{n+1} - c_{l,2}^{n+1}.$$

Therefore, taking advantage of the linearity of the involved forms, choosing $\boldsymbol{v} = \delta_t \mathcal{U}^{n+1}$ in (4.7c), and then applying Cauchy–Schwarz and Young inequalities, and multiplying the resulting inequality by Δt and summing over $n - 1$, we finally obtain

$$\mu_s C_{k,1} \|\mathcal{U}^n\|_{1,\Omega}^2 + \frac{\mu_s C_{k,1} \Delta t^2}{4} \sum_{m=0}^{n-1} \|\delta_t \mathcal{U}^{m+1}\|_{1,\Omega}^2$$

$$\leq C \left\{ \|\mathcal{U}^0\|_{1,\Omega}^2 + \sum_{m=0}^{n-1} \|\chi^{m+1}\|_{0,\Omega}^2 + \sum_{m=0}^{n-1} \|\boldsymbol{b}_1 - \boldsymbol{b}_2\|_{0,\Omega}^2 + \sum_{m=0}^{n-1} \|\mathbf{R}_{3,1} - \mathbf{R}_{3,2}\|_{0,\Omega}^2 \right\}, \quad (4.23)$$

where C is a constant independent of Δt. On the other hand, by taking $q = \mathcal{P}^{n+1}$ and $\psi = \chi^{n+1}$ in (4.7d) and (4.7e), respectively, and then, applying again the linearity of the bilinear forms and proceeding as in [77, Lemma 2.2], we arrive at the following estimate

$$\frac{1}{2\lambda_s} \|\chi^n\|_{0,\Omega}^2 + \frac{1}{2}\left(1 + \frac{\alpha}{\lambda_s}\right)\left(\|\mathcal{P}^n\|_{0,\Omega}^2 + \Delta t^2 \sum_{m=0}^{n-1} \|\delta_t \mathcal{P}^{m+1}\|_{0,\Omega}^2\right) + \frac{\kappa_1 \Delta t}{2\mu_f} \sum_{m=0}^{n-1} \|\mathcal{P}^{m+1}\|_{1,\Omega}^2$$

$$\leq \frac{1}{2\lambda_s} \|\chi^0\|_{0,\Omega}^2 + \frac{1}{2}\left(1 + \frac{\alpha}{\lambda_s}\right)\|\mathcal{P}^0\|_{0,\Omega}^2 + \left(\frac{(1+\alpha)^2}{2\lambda} + 1\right) \sum_{m=0}^{n-1} \|\mathcal{P}^{m+1}\|_{0,\Omega}^2$$

$$+ \frac{1}{2} \sum_{m=0}^{n-1} \|\tilde{R}_{4,1}^m - \tilde{R}_{4,2}^m\|_{0,\Omega}^2$$

$$+ \frac{\mu_f \Delta t}{2\kappa_1} \sum_{m=0}^{n-1} \|R_{4,1} - R_{4,2}\|_{0,\Omega}^2 + \frac{1}{2} \sum_{m=0}^{n-1} \|\mathcal{C}_p^{m+1}\|_{0,\Omega}^2$$

$$+ \frac{1}{2\mu_s C_{k,1}} \|\chi^{n+1}\|_{0,\Omega}^2 + \frac{\mu_s C_{k,1}}{2} \|\mathcal{U}^{n+1}\|_{1,\Omega}^2$$

$$+ \frac{1}{\mu C_{k,1}} \sum_{m=0}^{n-1} \|\chi^{m+1}\|_{0,\Omega}^2 + \frac{\mu_s C_{k,1} \Delta t^2}{4} \sum_{m=0}^{n-1} \|\delta_t \mathcal{U}^{m+1}\|_{1,\Omega}^2. \quad (4.24)$$

Now, for the diffusion-reaction problem, we apply the linearity of the bilinear forms in (4.7a)–(4.7b), with test functions $\mathcal{C}_p$ and $\mathcal{C}_l$, respectively, and then, proceeding similar to Lemma 4.1, we get

$$\|\mathcal{C}_p^n\|_{0,\Omega}^2 + \|\mathcal{C}_l^n\|_{0,\Omega}^2 + \Delta t^2 \sum_{m=0}^{n-1} (\|\delta_t \mathcal{C}_p^{m+1}\|_{0,\Omega}^2 + \|\delta_t \mathcal{C}_l^{m+1}\|_{0,\Omega}^2)$$

$$+ D^{\min} \Delta t \sum_{m=0}^{n-1} (|\mathcal{C}_p^{m+1}|_{1,\Omega}^2 + |\mathcal{C}_l^{m+1}|_{1,\Omega}^2)$$

$$\leq C \left(\|\mathcal{C}_p^0\|_{0,\Omega}^2 + \|\mathcal{C}_l^0\|_{0,\Omega}^2 + \sum_{m=0}^{n-1} \left(\|\tilde{R}_{1,1}^m - \tilde{R}_{1,2}^m\|_{0,\Omega}^2 + \|\tilde{R}_{2,1}^m - \tilde{R}_{2,2}^m\|_{0,\Omega}^2 \right) \right.$$

$$+ \frac{\Delta t}{2} \sum_{m=0}^{n-1} \left(\|R_{1,1} - R_{1,2}\|^2 \right.$$

$$+ \|R_{2,1} - R_{2,2}\|_{0,\Omega}^2) + \left(1 + \frac{\Delta t}{2}\right) \sum_{m=0}^{n-1} \left(\|\mathcal{C}_p^{m+1}\|_{0,\Omega}^2 + \|\mathcal{C}_l^{m+1}\|_{0,\Omega}^2 \right)$$

$$\left. + \sum_{m=0}^{n-1} \|\chi^{m+1}\|_{0,\Omega}^2 + \sum_{m=0}^{n-1} \|\mathcal{P}^{m+1}\|_{0,\Omega}^2 \right), \quad (4.25)$$

where $D^{\min} := \min\{D_p^{\min}, D_l^{\min}\}$. Finally, thanks to the inf-sup condition (4.6), it is possible to obtain a bound for $\|\chi^{n+1}\|_{0,\Omega}$ independent of λ_s, and then, combining (4.23)–(4.25), and then using Gronwall's lemma, it can be deduced that

$$
\begin{aligned}
&\|\mathcal{U}^{n+1}\|_{1,\Omega} + \|\mathcal{P}^{n+1}\|_{0,\Omega} + \|\chi^{n+1}\|_{0,\Omega} + \|\mathcal{C}_p^{n+1}\|_{0,\Omega} + \|\mathcal{C}_l^{n+1}\|_{0,\Omega} \\
&\quad + \|\mathcal{P}\|_{l^2(H^1(\Omega))} + \|\nabla\mathcal{C}_p\|_{l^2(L^2(\Omega))} + \|\nabla\mathcal{C}_l\|_{l^2(L^2(\Omega))} \\
&\leq C\sqrt{\exp(C_1)}\Bigg(\|\mathcal{U}^0\|_{1,\Omega} + \|\mathcal{P}^0\|_{0,\Omega} + \|\chi^0\|_{0,\Omega} + \|\mathcal{C}_p^0\|_{0,\Omega} + \|\mathcal{C}_l^0\|_{0,\Omega} \\
&\quad + \sum_{m=0}^{n} \|\boldsymbol{b}_1 - \boldsymbol{b}_2\|_{0,\Omega} \\
&\quad + \sum_{m=0}^{n} \left(\|\tilde{R}_{1,1}^m - \tilde{R}_{1,2}^m\|^2 + \|\tilde{R}_{2,1}^m - \tilde{R}_{2,2}^m\|^2 \right) \\
&\quad + \Delta t\|R_{1,1} - R_{1,2}\|_{0,\Omega}^2 + \Delta t\|R_{2,1} - R_{2,2}\|_{0,\Omega}^2 \\
&\quad + \|\mathbf{R}_{3,1} - \mathbf{R}_{3,2}\|_{0,\Omega}^2 + \sum_{m=0}^{n} \|\tilde{R}_{4,1}^m - \tilde{R}_{4,2}^m\|_{0,\Omega}^2 + \Delta t\|R_{4,1} - R_{4,2}\|_{0,\Omega}^2 \Bigg),
\end{aligned}
$$

from which, we can ensure the existence of at most one weak solution to the system (4.7a)–(4.7e). $\qquad\square$

4.5 Stability of the Linearised Coupled Problem

The following lemma establishes the continuous dependence on data for problem (4.7a)–(4.7e). Its proof follows similar arguments to those used in Lemmas 4.1, 4.2 and 4.7, and therefore we omit it here.

Lemma 4.8 *The solution* $(c_p^{n+1}, c_l^{n+1}, \boldsymbol{u}^{n+1}, p^{n+1}, \zeta^{n+1}) \in \mathrm{H}^1(\Omega) \times \mathrm{H}^1(\Omega) \times \mathbf{H}_\Gamma^1(\Omega) \times \mathrm{H}_\Sigma^1(\Omega) \times \mathrm{L}^2(\Omega)$ *of problem* (4.7a)–(4.7e) *satisfies*

$$
\begin{aligned}
&\|\boldsymbol{u}^{n+1}\|_{1,\Omega} + \|p^{n+1}\|_{0,\Omega} + \|\zeta^{n+1}\|_{0,\Omega} + \|p\|_{\ell^2(H^1(\Omega))} \\
&\quad + \|c_p^{n+1}\|_{0,\Omega} + \|c_l^{n+1}\|_{0,\Omega} + \|\nabla c_p\|_{\ell^2(L^2(\Omega))} \\
&\quad + \|\nabla c_l\|_{\ell^2(L^2(\Omega))} \leq \sqrt{\exp(C)}\Big\{ \|\boldsymbol{u}^0\|_{1,\Omega} + \|p^0\|_{0,\Omega} + \|\zeta^0\|_{0,\Omega} \\
&\quad + \|c_p^0\|_{0,\Omega} + \|c_l^0\|_{0,\Omega} + \|\boldsymbol{b}\|_{0,\Omega} \\
&\quad + \sum_{m=0}^{n} \left(\|\tilde{R}_1^m\|_{0,\Omega} + \|\tilde{R}_2^m\|_{0,\Omega} + \|\tilde{R}_4^m\|_{0,\Omega} \right) + \|\mathbf{R}_3\|_{0,\Omega} + \Delta t\|R_1\|_{0,\Omega} \\
&\quad + \Delta t\|R_2\|_{0,\Omega} + \Delta t\|R_4\|_{0,\Omega} \Big\},
\end{aligned}
$$

where $C > 0$ *is a constant independent of* λ_s.

Remark 4.1 – Although carrying out the solvability analysis of the linearised fully-continuous problem goes beyond the scope of this work, it is possible to extend the ideas presented here to establish that well-posedness using appropriate choices of Sobolev spaces, and performing a passage to the limit adapting to our problem the results from, e.g., [5] (which focus on reaction–diffusion–Brinkman problems).

– The solvability analysis of the fully-discrete problem associated with (4.7a)–(4.7e) can be established similarly to the semidiscrete-in-time case. More precisely, with the finite elements spaces specified in (5.1), we can define an appropriate fixed-point operator and prove that it is well-defined thanks to the well-posedness of each uncoupled problem (see a general form in, e.g., [64]). Then, by employing the continuous dependence in the fully-discrete case (which follows exactly as in Lemma 4.8) in combination with the analysis from [5, Sect. 5.3], we can prove the continuity of the fixed-point operator described above. Finally, the desired result follows from an application of Brouwer's fixed–point theorem.

– Given the approximation properties of the finite element spaces specified in (5.1) (and recalled in, e.g., [60]), and following the steps given by [77, Sect. 4], it is possible to derive an asymptotic $\mathcal{O}(h)$ convergence for the proposed method. This is also verified for the nonlinear case, as shown numerically in Sect. 6.

– The convergence properties are also robust with respect to incompressibility of the solid phase.

– We stress that the arguments presented in this section are unfortunately not readily generalised to arbitrary hyperelastic materials, nor a generic initial guess for the Newton–Raphson loop. In all of the numerical tests performed below, this has not shown to be a problem in practice. Still, the lack of a global existence result makes it is possible for the model to be increasingly difficult in the simulation of other scenarios of interest, such as pathological ones.

5 A Finite Element Formulation

5.1 Discretisation of the Nonlinear Problem

In order to define a Galerkin finite element method we denote by $\{\mathcal{T}_h\}_{h>0}$ a shape-regular family of partitions of $\bar{\Omega}$, conformed by tetrahedra (or triangles in 2D) K of diameter h_K, with mesh size $h := \max\{h_K : K \in \mathcal{T}_h\}$. Given an integer $k \geq 1$ and a subset S of $\mathbb{R}^d$, $d = 2, 3$, by $\mathbb{P}_k(S)$ we will denote the space of polynomial functions defined locally in S and being of total degree up to k. Let us also denote by $b_K := \varphi_1 \varphi_2 \varphi_3$ a $\mathbb{P}_3$ bubble function in K, where φ_1, φ_2, φ_3 are the barycentric coordinates of the triangle K (in 3D the bubble is a quartic polynomial). Then the finite-dimensional subspaces for the pathogen and leukocyte concentrations $W_h \subseteq H^1(\Omega)$, displacement $\mathbf{V}_h \subseteq \mathbf{H}^1_\Gamma(\Omega)$, porous fluid pressure $Q_h \subseteq H^1_\Sigma(\Omega)$, and nominal porosity $\Phi_h \subseteq L^2(\Omega)$ are defined, respectively, as follows

$$
\begin{aligned}
W_h &:= \{w_h \in C(\overline{\Omega}) : w_h|_K \in \mathbb{P}_1(K)^d, \ \forall K \in \mathcal{T}_h\}, \\
\mathbf{V}_h &:= \{\boldsymbol{v}_h \in \boldsymbol{C}(\overline{\Omega}) : \boldsymbol{v}_h|_K \in [\mathbb{P}_1(K) \oplus \text{span}\{b_K\}]^d \ \forall K \in \mathcal{T}_h, \ \boldsymbol{v}_h|_\Gamma = \boldsymbol{0}\}, \\
Q_h &:= \{q_h \in C(\overline{\Omega}) : q_h|_K \in \mathbb{P}_1(K), \ \forall K \in \mathcal{T}_h, \ q_h|_\Sigma = 0\}, \\
\Phi_h &:= \{\psi_h \in C(\overline{\Omega}) : \psi_h|_K \in \mathbb{P}_1(K), \ \forall K \in \mathcal{T}_h\}.
\end{aligned} \tag{5.1}
$$

The pair $(\mathbf{V}_h, \Phi_h)$ is the well-known MINI-element, which is inf-sup stable in the context of saddle-point Stokes equations in their velocity-pressure formulation [28].

Then the fully discrete problem arises from (3.2) and for each time step n, we perform inner Newton–Raphson iterations from $k = 0, \ldots$ seeking $(\delta c_{p,h}^{k+1}, \delta c_{l,h}^{k+1}, \delta \boldsymbol{u}_h^{k+1}, \delta p_h^{k+1}, \delta \phi_{f,h}^{k+1}) \in$

$W_h \times W_h \times V_h \times Q_h \times \Phi_h =: \mathbf{H}_h$ solutions to the unsymmetric matrix system

$$
\begin{bmatrix}
\mathcal{A}_1 & \mathcal{B}'_1 & \mathcal{B}'_2 & \mathbf{0} & \mathcal{B}'_3 \\
\mathcal{B}_1 & \mathcal{A}_2 & \mathcal{B}'_4 & \mathbf{0} & \mathcal{B}'_5 \\
\mathbf{0} & \mathbf{0} & \mathcal{A}_3 & \mathcal{C}'_1 & \mathbf{0} \\
\mathcal{C}_2 & \mathbf{0} & \mathcal{C}_1 & \mathcal{A}_4 & \mathcal{C}'_3 \\
\mathbf{0} & \mathbf{0} & \mathcal{C}_4 & \mathbf{0} & -\mathcal{A}_5
\end{bmatrix}
\begin{bmatrix}
\delta C_p^{k+1} \\
\delta C_l^{k+1} \\
\delta U^{k+1} \\
\delta P^{k+1} \\
\delta \Phi_f^{k+1}
\end{bmatrix}
=
\begin{bmatrix}
\mathcal{F}_{1,h}^{k,n} \\
\mathcal{F}_{2,h}^{k,n} \\
\mathcal{F}_{3,h}^{k} \\
\mathcal{F}_{4,h}^{k,n} \\
\mathcal{F}_{5,h}^{k}
\end{bmatrix},
\tag{5.2}
$$

where the entries δC_p^{k+1}, δC_l^{k+1}, δU^{k+1}, δP^{k+1} and $\delta \Phi_f^{k+1}$ in the independent vector variable are the vectors containing all internal degrees of freedom associated with the discrete incremental solutions for all fields, and the operators in calligraphic letters appearing in the coefficient matrix and load vector from (5.2) are induced by the corresponding bilinear forms and linear functionals in (3.3). The functionals with superscript n on the right-hand side vector indicate that they also receive contributions from the backward Euler time-discretisation.

5.2 Schur Complement Based Robust Preconditioner

The numerical solution of problem (5.2) through direct methods is not feasible for large systems, which is a natural consequence of considering finer meshes for 3D geometries, needed to better capture anatomical details. This is the standard scenario in which Krylov space methods are the most useful, more specifically a GMRES method due to the indefinite and non-symmetric nature of the problem [69]. Still, scalable solvers require the construction of a robust preconditioner that allows for the Krylov iterations to remain roughly constant whenever (i) the amount of processors is increased and (ii) the mesh is refined. In this section we propose a preconditioner based on a two-level nested Schur complement inspired by the multiphysics nature of the model. If we consider a block matrix $\mathbf{M}$ given by the general structure

$$
\mathbf{M} = \begin{bmatrix} \mathbf{A} & \mathbf{B}_1 \\ \mathbf{B}_2 & \mathbf{C} \end{bmatrix},
$$

with $\mathbf{A}$ invertible, a Gauss elimination procedure yields

$$
\mathbf{M} = \begin{bmatrix} \mathbf{I} & \mathbf{0} \\ \mathbf{B}_2\mathbf{A}^{-1} & \mathbf{I} \end{bmatrix}
\begin{bmatrix} \mathbf{A} & \mathbf{0} \\ \mathbf{0} & \mathbf{C} - \mathbf{B}_2\mathbf{A}^{-1}\mathbf{B}_1 \end{bmatrix}
\begin{bmatrix} \mathbf{I} & \mathbf{A}^{-1}\mathbf{B}_1 \\ \mathbf{0} & \mathbf{I} \end{bmatrix}.
\tag{5.3}
$$

We note that if $\mathbf{C}$ is invertible, the same procedure can be applied with respect to it. Schur complement based preconditioners enjoy excellent theoretical properties, as the preconditioned system possesses at most 3 distinct eigenvalues [57], implying that it converges in at most 3 iterations of a Krylov subspace method, but this is seldom true in practice as the Schur complement block $\mathbf{S} = \mathbf{C} - \mathbf{B}_2\mathbf{A}^{-1}\mathbf{B}_1$ is computationally expensive to compute. Two complementary strategies to circumvent this problem are (i) to consider the full/lower triangular/upper triangular/diagonal part of (5.3) and (ii) to approximate $\mathbf{S}$. In turn, two standard approaches for approximating $\mathbf{S}$ are the SIMPLE preconditioner given by $\mathbf{S} \approx \mathbf{C} - \mathbf{B}_2\text{diag}(\mathbf{A})^{-1}\mathbf{B}_1$ and the block diagonal approximation $\mathbf{S} \approx \mathbf{C}$ (for other possibilities and their comparison see, e.g., the comprehensive review [35]).

On the first level of the proposed preconditioner, we split the variables into poroelastic and chemotaxis, denoted by poro $= (\boldsymbol{u}, p, \phi_f)$ and chem $= (c_p, c_l)$ respectively, and use

this to write the linearised problem as

$$\mathbf{J} = \begin{bmatrix} \mathbf{J}_{\text{poro}} & \mathbf{J}_{\text{poro, chem}} \\ \mathbf{J}_{\text{chem, poro}} & \mathbf{J}_{\text{chem}} \end{bmatrix}, \tag{5.4}$$

where each block is given by

$$\mathbf{J}_{\text{poro}} = \begin{bmatrix} \mathcal{A}_3 & \mathcal{C}_1' & \mathbf{0} \\ \mathcal{C}_1 & \mathcal{A}_4 & \mathcal{C}_3' \\ \mathcal{C}_4 & \mathbf{0} & -\mathcal{A}_5 \end{bmatrix}, \quad \mathbf{J}_{\text{chem}} = \begin{bmatrix} \mathcal{A}_1 & \mathcal{B}_1' \\ \mathcal{B}_1 & \mathcal{A}_2 \end{bmatrix},$$

$$\mathbf{J}_{\text{poro,chem}} = \begin{bmatrix} \mathbf{0} & \mathbf{0} \\ \mathcal{C}_2 & \mathbf{0} \\ \mathbf{0} & \mathbf{0} \end{bmatrix}, \quad \mathbf{J}_{\text{chem,poro}} = \begin{bmatrix} \mathcal{B}_2' & \mathbf{0} & \mathcal{B}_3' \\ \mathcal{B}_4' & \mathbf{0} & \mathcal{B}_5' \end{bmatrix}.$$

Using (5.3) we can write the inverse of (5.4) as

$$\mathbf{J}^{-1} = \begin{bmatrix} \mathbf{I} & -\mathbf{J}_{\text{poro}}^{-1}\mathbf{J}_{\text{poro,chem}} \\ \mathbf{0} & \mathbf{I} \end{bmatrix} \begin{bmatrix} \mathbf{J}_{\text{poro}}^{-1} & \mathbf{0} \\ \mathbf{0} & (\mathbf{J}_{\text{chem}} - \mathbf{J}_{\text{chem,poro}}\mathbf{J}_{\text{poro}}^{-1}\mathbf{J}_{\text{poro,chem}})^{-1} \end{bmatrix}$$
$$\begin{bmatrix} I & \mathbf{0} \\ -\mathbf{J}_{\text{chem,poro}}\mathbf{J}_{\text{poro}}^{-1} & \mathbf{0} \end{bmatrix}.$$

Still, the application of this preconditioner requires applying $\mathbf{J}_{\text{poro}}^{-1}$, for which we consider an additional splitting between displacement and the pair (pressure, nominal porosity) denoted as $\boldsymbol{u} - \Pi$, with $\Pi = (p, \phi_f)$. We can apply the same argument to the block $\mathbf{J}_{\text{poro}}$, now written as

$$\mathbf{J}_{\text{poro}} = \begin{bmatrix} \mathbf{J}_{\boldsymbol{u}} & \mathbf{J}_{\boldsymbol{u},\Pi} \\ \mathbf{J}_{\Pi,\boldsymbol{u}} & \mathbf{J}_{\Pi} \end{bmatrix},$$

by making use of the invertibility of the displacement block $\mathbf{J}_{\boldsymbol{u}}$, where the sub-blocks are given by

$$\mathbf{J}_{\boldsymbol{u}} = \mathcal{A}_3, \quad \mathbf{J}_{\Pi} = \begin{bmatrix} \mathcal{A}_4 & \mathcal{C}_3' \\ \mathbf{0} & -\mathcal{A}_5 \end{bmatrix}, \quad \mathbf{J}_{\boldsymbol{u},\Pi} = \begin{bmatrix} \mathcal{C}_1' & \mathbf{0} \end{bmatrix}, \quad \mathbf{J}_{\Pi,\boldsymbol{u}} = \begin{bmatrix} \mathcal{C}_1 \\ \mathcal{C}_4 \end{bmatrix}.$$

This idea has been applied in [33] for an FSI problem, and in [48] for the Boussinesq equations. The equations governing (c_p, c_l) are of parabolic type and so their approximation does not pose a challenge, which indicates that the main difficulty lies in the poroelastic block approximation. Motivated by this, the proposed preconditioner is given by the following components:

– On the first level we consider a lower-triangular Schur decomposition and on the second level we consider a full one.
– The "chem" block is approximated by the action of the HYPRE-BoomerAMG [81] preconditioner.
– Both blocks in the second level are approximated by an inexact GMRES solver preconditioned by an additive Schwarz method with a direct solver in each subdomain (using the MUMPS library [4]).

The inexactness is given by a relative tolerance of 0.1, and we highlight that an inexact solver in the sub-blocks gives rise to a preconditioner that changes from one iteration to the next one. This requires the use of a flexible GMRES algorithm (fGMRES) [68]. The use of an additive Schwartz preconditioner, or in general a domain decomposition one, alleviates

the deteriorating scalability of AMG preconditioners for higher-order elements, in this case required by the displacement to satisfy an appropriate discrete inf-sup condition.

We close this section by noting that the choice of the type of Schur decomposition is not arbitrary. For this, we consider exact, lower triangular Schur complement preconditioners at both levels. In this way, the preconditioner adopts the following form

$$
\mathbf{P} = \begin{bmatrix} \mathbf{P}_{\text{poro}} & \mathbf{0} \\ \mathbf{J}_{\text{chem,poro}} & \mathbf{S}_{\text{chem}} \end{bmatrix},
$$

where

$$
\mathbf{P}_{\text{poro}} = \begin{bmatrix} \mathbf{J}_u & \mathbf{0} \\ \mathbf{J}_{\Pi,u} & \mathbf{S}_{\Pi} \end{bmatrix}, \quad \mathbf{S}_{\Pi} = \mathbf{J}_{\Pi} - \mathbf{J}_{\Pi,u}\mathbf{J}_u^{-1}\mathbf{J}_{u,\Pi},
$$

$$
\mathbf{S}_{\text{chem}} = \mathbf{J}_{\text{chem}} - \mathbf{J}_{\text{chem,poro}}\mathbf{J}_{\text{poro}}^{-1}\mathbf{J}_{\text{poro,chem}}.
$$

After algebraic manipulations, it can be seen that the preconditioned system is given by

$$
\mathbf{P}^{-1}\mathbf{J} = \begin{bmatrix} \mathbf{P}_{\text{poro}}^{-1}\mathbf{J}_{\text{poro}} & \mathbf{P}_{\text{poro}}^{-1}\mathbf{J}_{\text{poro,chem}} \\ \mathbf{S}_{\text{chem}}^{-1}\mathbf{J}_{\text{chem,poro}}(\mathbf{I} - \mathbf{P}_{\text{poro}}^{-1}\mathbf{J}_{\text{poro}}) & \mathbf{S}_{\text{chem}}^{-1}(\mathbf{J}_{\text{chem}} - \mathbf{J}_{\text{chem,poro}}\mathbf{P}_{\text{poro}}^{-1}\mathbf{J}_{\text{poro,chem}}) \end{bmatrix} \quad (5.5)
$$

where

$$
\mathbf{P}_{\text{poro}}^{-1}\mathbf{J}_{\text{poro}} = \begin{bmatrix} \mathbf{I} & \mathbf{J}_u^{-1}\mathbf{J}_{u,\Pi} \\ \mathbf{0} & \mathbf{I} \end{bmatrix}.
$$

The preconditioned system does not exhibit the expected property of having a small number of eigenvalues. This is mainly due to the use of a preconditioner instead of an exact inverse, where $\mathbf{P}_{\text{poro}} \neq \mathbf{J}_{\text{poro}}$. If such blocks coincide, then we would have

$$
\mathbf{P}^{-1}\mathbf{J} = \begin{bmatrix} \mathbf{I} & \mathbf{J}_{\text{poro}}^{-1}\mathbf{J}_{\text{poro,chem}} \\ \mathbf{0} & \mathbf{I} \end{bmatrix}, \quad (5.6)
$$

which justified the use of an exact Schur preconditioner at the second level. This results in a preconditioned problem with only one eigenvalue.

6 Computational Experiments

We now turn to the presentation of numerical examples serving to illustrate the performance of the finite element scheme and to examine further the main features of the model. All routines have been implemented using the open source finite element library FEniCS [1]. A fixed tolerance of 10^{-6} is used on the residuals for the convergence criterion of the Newton–Raphson iterative algorithm. We highlight that the error control of multiphysics problems is not trivial, for example in [16] as an error they use the norm of the increment, whereas in [80] they use the norm of the residual. We prefer the norm of the residual, as having an increment going to zero might mean stagnation and not convergence. Still, this can be improved by checking the error in each physics separatedly.

6.1 Sensitivity Analysis of Model Parameters

This section presents the influence of some parameters on the dynamics of the proposed model to highlight the coupling mechanisms between the poroelastic component (2.2) and

the advection-reaction-diffusion component (2.4) describing pathogens and immune system dynamics, respectively. The analyses were performed in a one dimensional version of the fully coupled model given by Eqs. (2.2)–(2.4) considering a domain $\Omega \in [0, 8]$ cm. An initial pathogen concentration of $c_{p,0} = 0.001$ was considered in the middle of the domain $x \in [3.95, 4.05]$ to start the infection, whereas in the remaining domain $c_{p,0} = 0$ was used. Throughout the domain we also consider the following initial conditions: $c_{l,0} = 0.003$, $\phi_0 = 0.2$, and $p_0 = 0$. The following boundary conditions were considered: $\boldsymbol{u} = \boldsymbol{0}$ on the left at $x = 0$, and $p = 0$ was prescribed at the right end at $x = 8$ cm of the domain.

A simplified sensitivity analysis varying one parameter at a time with respect to the reference parameters reported in Table 1 was performed. We limit the presentation of these results to only a few parameters and variables divided into three cases that highlight the couplings of the model. Young's modulus E, associated with the mechanical part, was investigated for the first case. In the second and third cases, associated with the immune response of the model, both phagocytosis rate, λ_{lp}, and pathogen's reproduction rate, γ_P, were studied. These parameters were chosen because they better highlighted the couplings in the model. They are also related to critical biological responses depending on their values. Changes in the value of γ_P, for example, can be associated with pathogens with distinct proliferation abilities; changes in the value of λ_{lp} can describe the ability of leukocytes in dealing with the invading pathogen; whereas changes in E represent tissues with different stiffness.

In all the three cases, the investigated parameter (E, λ_{lp}, or γ_P) had its value doubled and halved with respect to the reference value reported in Table 1. To study these three scenarios, we assume that pathogens are responsible for triggering the inflammatory response. For this reason, the instant in which pathogens' concentration reaches its peak is used as a reference to collect data from the other variables of interest.

Figure 2 shows the results of the sensitivity analysis. The time in which pathogens concentration reaches its maximum was distinct for each scenario only for the analysis of the influence of pathogen's reproduction rate (cf. Fig. 2, third line), occurring after 12 days, six days, and 24 days, respectively, since the start of infection. For the analysis of λ_{lp} and λ_{pl}, the instant of time at which the pathogens reach the maximum was 12 days since the start of infection.

The plots in the first row of Fig. 2 presents the results for varying tissue stiffness. A stiffer tissue will imply a lower capacity to deform and accumulate fluid. With a smaller amount of fluid in the infected region, the concentration of pathogens and leukocytes in the tissue increases (Fig. 2, top left), i.e., the same amount of pathogens in the region is divided by a smaller fluid volume.

The second row of panels in Fig. 2 presents the results for varying the phagocytosis rate, λ_{lp}. A reduction in λ_{lp} value can be related to a scenario in which the immune system is ineffective in dealing with the invading pathogen. This could be explained by immunodeficiency, for example. In this context, the concentration of pathogens will reach a higher and faster peak of infection for smaller values of λ_{lp}. The lower capacity of phagocytosis by leukocytes leads to a considerable increase in the concentration of pathogens (Fig. 2, centre left). The increase in pathogens' concentration induces an increase in the capillary permeability, which allows a more significant accumulation of fluid in the infected region (Fig. 2 centre middle). The accumulation of fluid in the region causes the pressure to increase. As a consequence of these events, the deformation suffered by the tissue is greater than the one observed for higher values of λ_{lp} (Fig. 2 centre right).

Note that an increase in γ_P can be interpreted as a pathogen that can reproduce faster due to its intrinsic biological characteristics or due to the presence of favourable conditions (abundance of nutrients or temperature, for example). In fact, as the bottom row of Fig. 2

Table 1 Example 1: Reference parameters of the model to be used in Sect. 6.1

Parameter	Units	Description	References	Parameter	Units	Description	References
$E = 60$	kg/cm s^2	Young modulus	Estimated	$\lambda_{lp} = 1.5$	1/d c	Phagocytosis rate	Estimated
$\nu = 0.35$	–	Poisson coefficient	Estimated	$\bar{\lambda}_{lp} = \lambda_{lp}/\phi_0$	1/d c	Relative phagocytosis rate	Estimated
λ_s	kg/cm s^2	First Lamé parameter		$\lambda_{pl} = 7.1$	1/d c	Leukocytes migration rate	Estimated
μ_s	kg/cm s^2	Shear module		$\bar{\lambda}_{pl} = \lambda_{pl}/\phi_0$	1/d c	Relative leukocytes migration	
$\rho_f = 1$	kg/cm^3	Fluid phase density	Estimated	$\pi_i = 10$	mmHg	Interstitial oncotic pressure	[61]
$\rho_s = 2e^{-3}$	kg/cm^3	Solid phase density	[11]	$\pi_c = 20$	mmHg	Capillary oncotic pressure	[61]
$\alpha = 0.25$	–	Biot modulus	Estimated	$\sigma_0 = 0.91$	–	Osmotic reflection coefficient	[61]
$\phi_0 = 0.2$	–	Initialfluid phase	[13]	$L_{bp} = 1e4$	1/c	Pathogen influence on permeability	Estimated
$D_p = 1e^{-3}$	cm^2/d	Pathogen diffusion	Estimated	$P_c = 20$	mmHg	Capillary pressure	[61]
$\bar{D}_p = D_p/\phi_0$	cm^2/d	Relative pathogen diffusion		$L_{p0} = 3.6e^{-8}$	cm/s mmHg	Hydraulic permeability	[61]
$D_l = 5e^{-2}$	cm^2/d	Leukocyte diffusion	Estimated	$\ell_0 = 6.82e^{-5}$	1/s	Normal lymphatic flow	Estimated
$\bar{D}_l = D_l/\phi_0$	cm^2/d	Relative leukocyte diffusion		$k_m = 6.5$	mmHg	Half life of lymphatic flow	Estimated
$\mathcal{X} = 1e^{-2}$	cm^2/d c	Chemotaxis	Estimated	$nHill = 1$	–	Hill coefficient	Estimated
$\bar{\mathcal{X}} = \mathcal{X}/\phi_0$	cm^2/d c	Relative chemotaxis		$V_{max} = 200$	–	Max lymphatic flow	Estimated
$\gamma_p = 1.2e^{-1}$	1/d	Pathogen reproduction rate	Estimated	$K = 2.5e^{-7}$	cm^2/s mmHg	Permeability	[61]
$\bar{\gamma}_p = \gamma_p/\phi_0$	1/d	Relative pathogen reproduction rate		$(S/V) = 174$	1/cm	Vessel area per volume unit	[61]
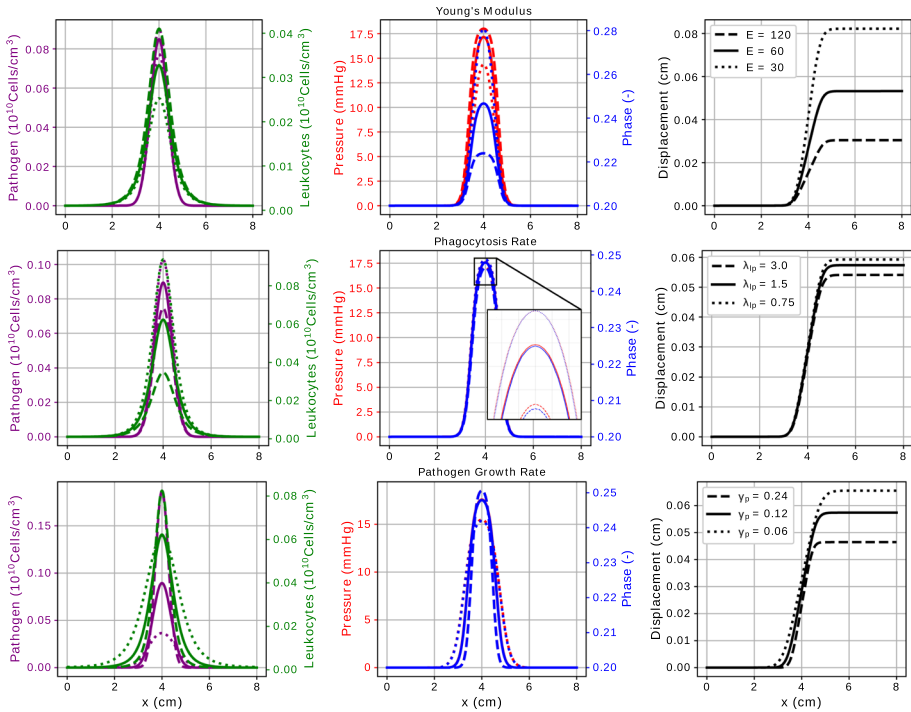
Fig. 2 Example 1: The interaction of immune response and mechanical parts of the model is evaluated using Young's modulus (E, first line), phagocytosis rate (λ_{lp}, second line) and pathogen reproduction rate (γ_P, last line) at the time instant in which the peak pathogen concentration is reached. For each of these three parameters, three scenarios are evaluated and plotted as distinct curves in each graphic: $E = 60$ (scenario 1, solid line), $E = 120$ (scenario 2, dashed line) and $E = 30$ (scenario 3, dotted line); $\lambda_{lp} = 1.5$ (scenario 1, solid line), $\lambda_{lp} = 3.0$ (scenario 2, solid line) and $\lambda_{lp} = 0.75$ (scenario 3, solid line); $\gamma_P = 0.12$ (scenario 1, solid line), $\gamma_P = 0.24$ (scenario 2, dashed line), $\gamma_P = 0.06$ (scenario 3, dotted line). The graphics in the left and in the middle columns are composed of two ordinate $y-$axes. In the first column, the left $y-$axis represents the concentration of pathogens and the right $y-$axis the concentration of leukocytes. The second column presents the pressure field and the fraction of fluid phase, respectively, on the left and right $y-$axes. The third column represents the deformation field on a single $y-$axis. All figures represent, on the $x-$axis, the tissue size in centimetres

shows, the peak of infection was higher and faster for larger γ_P values, as expected. However, counter-intuitively, high values of γ_P are associated with small deformations and small regions of oedema. As a result of more pathogens, the capillary permeability increases to allow more leukocytes to enter into the tissue (Fig. 2, bottom left). The rapid increase in the concentration of leukocytes contained the infection quickly, preventing pathogens from remaining in the tissue long enough to spread. Since the time pathogens stay in the tissue is short, as well as the region in which they spread, the deformation suffered by the tissue also decreases (Fig. 2, bottom right).

In the third scenario, with the small value of $\gamma_P = 0.06$, the peak of infection only occurs 24 days after the invasion begins, which leads to a weak inflammatory response. Thus, the concentration of leukocytes is reduced. The low leukocyte concentration results in a long time to remove pathogens that can spread over a larger region. The weak immune response results in more deformation when compared to the cases with faster pathogen dynamics, which highlights the couplings and strong nonlinearities in the model.
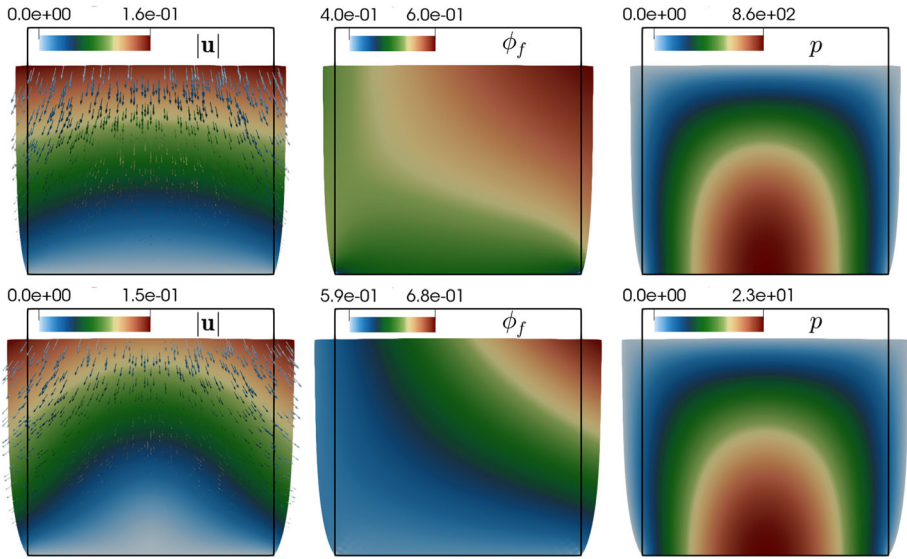
Fig. 3 Example 2: Compression and drainage of a porous structure. Approximate displacement magnitude, Lagrangian porosity, and fluid pressure, on the deformed configuration and computed at $t = 0.5$ with $\nu = 0.33$ (top) and $\nu = 0.495$ (bottom)

For this test we have also used the FEniCS environment along with the direct solver MUMPS.

6.2 Example 2: Compression and Drainage of a Poroelastic Sample

With the aim of illustrating the coupling between poroelastic deformation and fluid flow using the formulation (2.2a)–(2.2c) and in the absence of the immune system chemotaxis, we simulate the incremental compression of a box $\Omega = (0, 1)^2 \, \text{m}^2$. The bottom edge of the boundary constitutes Γ (where according to (2.6a), the deformation is zero and we impose zero fluid flux), whereas Σ is conformed by the top edge (where a sinusoidal-in-time distributed traction $\boldsymbol{t}_\Sigma = 2000 \sin(\pi t)\boldsymbol{n}$ is applied and a constant fluid pressure $p_{\text{in}} = 0.2 \, \text{MPa}$ is considered) as well as the vertical walls (where we prescribe zero traction and zero fluid pressure). We employ a non-homogeneous initial Lagrangian porosity that is not symmetric with respect to the centre of mass of the domain, given by $\phi_0(\boldsymbol{x}) = \frac{3}{5} + \frac{1}{10} \sin(x_1 x_2)$, the isotropic power-law porosity-dependent permeability, a compressible neo–Hookean strain energy density yielding the nominal effective stress $\mathbf{S}_{\text{eff}} = \mu_s(\mathbf{F}^{\text{t}} - \mathbf{F}^{-1}) + \lambda_s \ln J \mathbf{F}^{-1}$, and the parameters

$$E = 10^4 \, \text{kg/ms}^2, \quad \nu \in [0.2, 0.499999], \quad \mu_s = \frac{E}{2(1 + \nu)},$$

$$\lambda_s = \frac{E\nu}{(1 + \nu)(1 - 2\nu)}, \quad \boldsymbol{b} = \mathbf{0}, \quad \ell = 0,$$

$$\rho_s = 2 \cdot 10^{-3} \, \text{kg/m}^3, \quad \rho_f = 10^{-3} \, \text{kg/m}^3, \quad \alpha = 0.25,$$

$$\mu_f = 10^{-3} \, \text{m}^2/\text{s}, \quad \kappa_0 = 10^{-5} \, \text{m}^2.$$
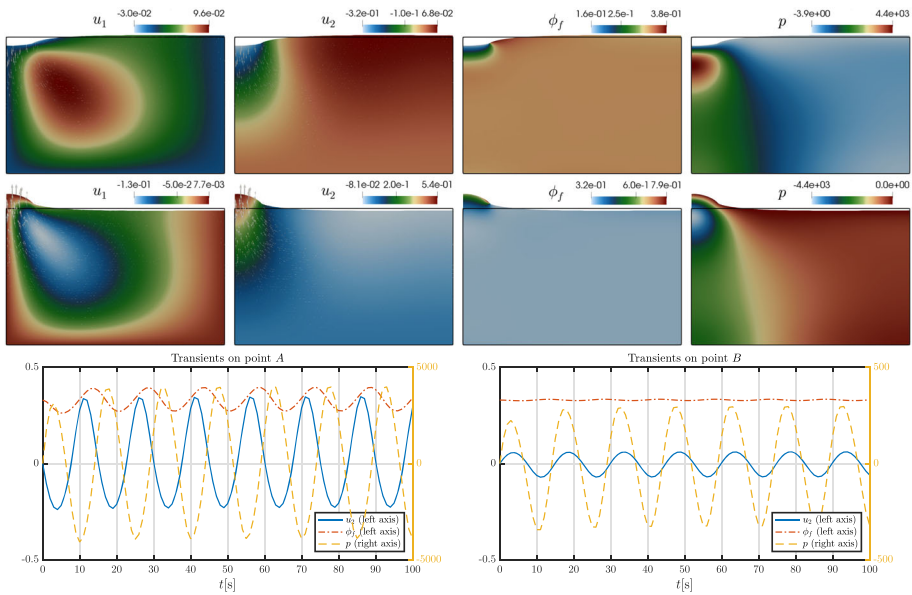
Fig. 4 Example 2: Compression benchmark. Approximate displacement components, Lagrangian porosity, and fluid pressure, on the deformed configuration and computed at $t = 34$ (top) and $t = 41$ (middle), and transients of field variables at points A and B (bottom)

The scheme characterised by the finite element spaces in (5.1) is used on a crossed-shaped uniform mesh with 10,000 cells, and the coupled system is simulated until $t_{\text{final}} = 1$ s using a constant time step $\Delta t = 0.1$ s. The system is considered initially at rest ($\boldsymbol{u}(0) = \boldsymbol{0}$, $p(0) = 0$, $\phi_f(0) = \phi_0$). This test also serves to assess the robustness of the method. We run a set of simulations varying the Poisson ratio from 0.2 to 0.499999. Regardless of the parameter regime, the numerical results do not show spurious oscillations of pressure, nor unexpectedly small displacements or nonphysical distortions or checker-board patterns in the porosity field. In Fig. 3 we plot deformed geometries and field variables showing the progressive compression of the porous block over three time instants, and using $\nu = 0.33$ and $\nu = 0.495$. As expected, the fluid pore pressure does not have a uniform distribution, and it moves toward Γ on the bottom edge.

In addition, we perform a benchmark test where again a time-harmonic loading defined by $\boldsymbol{t}_\Sigma = \frac{1}{5}(\lambda_s + 2\mu_s)\sin(\frac{2\pi}{15}t)\boldsymbol{n}$ is applied, now only on part of the top edge of the box $\Omega = (0, 8) \times (0, 5)\,\text{m}^2$ (on the segment $0 \leq x_1 \leq 1$ m, $x_2 = 5$ m). The setup of this validation example proceeds similarly as in [49, Sect. 4.2] (see also [84, Sect. 4.2] and [51, 65]). The boundary conditions in these references permit drainage (fixing a zero fluid pressure) on the whole top lid, setting zero fluid flux elsewhere on the boundary, the bottom edge is clamped (imposing zero displacement) while the vertical walls are on rollers (only the horizontal displacement is set to zero), and the remainder of the top edge is traction-free. The parameter values that change with respect to the previous case are

$$E = 3 \cdot 10^4\,\text{N/m}^2,\ \nu = 0.2,\ \alpha = 1,\ \kappa_0 = 10^{-8}\,\text{m}^2,\ \phi_0 = 0.33,\ t_{\text{final}} = 100\,\text{s},\ \Delta t = 1\,\text{s},$$

and we now use the normalised and isotropic Kozeny–Carman porosity-dependent permeability. For this test the mesh is unstructured and graded near the top-left corner. Figure 4 shows snapshots of the approximated field variables at times $t = 4, 12, 16$ s and the bot-
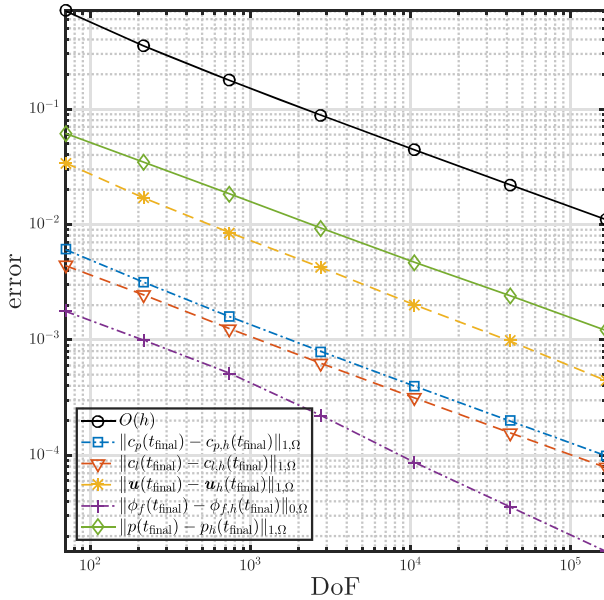
Fig. 5 Example 3: Error decay with respect to the number of degrees of freedom, computed between approximate solutions computed with a first-order method and manufactured solutions (6.1), at the final adimensional time $t_{final} = 0.03$

tom panels also portray transients of the vertical displacement and porosity recorded at two locations (node A $\approx$ (0.5,4.5), directly below the centre of the footing strip and node B $\approx$ (8.0,4.5) approximately at the same height but on the right wall). These plots show the same qualitative behaviour encountered in, e.g., [51].

6.3 Example 3: Errors with Respect to Manufactured Solutions

Since there is no analytical solution currently available for the coupled system (2.2a)–(2.4b), the accuracy of the finite element discretisation is investigated using the following closed-form manufactured solutions

$$c_p = t[0.3 \exp(x_1) + 0.1 \cos(\pi x_1) \cos(\pi x_2)], \quad c_l = t[0.3 \exp(x_1) + 0.1 \sin(\pi x_1) \sin(\pi x_2)],$$

$$\boldsymbol{u} = 0.25t \begin{pmatrix} \sin(\pi x_1) \cos(\pi x_2) + \frac{x_1^2}{\lambda_s} \\ -\cos(\pi x_1) \sin(\pi x_2) + \frac{x_2^2}{\lambda_s} \end{pmatrix},$$

$$p = t \sin(\pi x_1 x_2) \cos(\pi x_1 x_2), \quad \phi_0 = 0.6 + 0.1 \sin(x_1 x_2), \tag{6.1}$$

and $\phi_f = J - 1 + \phi_0$, defined on the unit square domain $\Omega = (0, 1)^2$. Together with the strong form of the governing equations, these exact solutions are used to obtain the load and source right-hand side terms. For simplicity we impose Dirichlet boundary conditions for the concentrations c_p, c_l whereas mixed boundary conditions are considered for the displacement and fluid pressure. On the left side of the boundary Γ, we prescribe the exact displacement from (6.1) and an exact traction $\mathbf{P}\boldsymbol{n}$ on the remainder of the boundary, Σ. The fluid pressure is constrained to match the exact one on Σ and an exact fluid pressure flux is imposed on Γ.

We use the same neo–Hookean material law as in Example 1, and employ the isotropic Kozeny–Carman permeability $\boldsymbol{\kappa}_{\text{iso}}^{\text{KC}}$. The following parameter values are selected

$$\lambda_s = 36.4, \quad \mu_s = 22.1,$$
$$\rho_s = \rho_f = \mu_f = \kappa_0 = L_{p0} = L_{bp} = L_{br} = v_{\max} = \gamma_p = \gamma_l = c_l^{\max} = 1,$$
$$\alpha = 0.5,$$
$$\mathbf{D}_p = 0.9\mathbf{I}, \quad \mathbf{D}_l = 0.8\mathbf{I},$$
$$\sigma_0 = \lambda_{lp} = \lambda_{pl} = \mu_l = l_0 = p_0 = \pi_i = k_m = \pi_c = \chi = p_c = S/V = 1, \quad n = 2,$$

they are all regarded adimensional and do not have physical relevance in this case, as we will be simply testing the convergence of the finite element solutions.

We generate successively refined simplicial grids and use a sufficiently small (non dimensional) time step $\Delta t = 0.01$ and simulate a sufficiently short time horizon $t_{\text{final}} = 3\Delta t$, to guarantee that the error produced by the time discretisation does not dominate. Errors between the approximate and exact solutions are plotted against the number of degrees of freedom in Fig. 5. This error history plot confirms the optimal convergence of the finite element scheme (in this case, first order) given by the Remark 4.1, for all variables in their respective norms, where a slightly better rate, of about 1.3, is seen for the porosity. In addition, the average iteration count for the Newton–Raphson method (for each refinement level and for all time steps) is five.

6.4 Example 4: Localisation of Oedema Regions

In the next test we present and discuss the coupling dynamics of the model (2.2)–(2.4), considering a two-dimensional domain $\Omega = (0, 4) \times (0, 4)$ cm^2, and a time step size of $\Delta t = 0.1$ days. The parameters described in the Table 1 were used. Boundary conditions were applied as follows: $\boldsymbol{u} = \boldsymbol{0}$ on the left edge, and $p = 0$ for the right, top and bottom edges of the domain, and the following initial conditions were used: $c_{p,0} = 0.001$ in the region $(x_1 - 2)^2 + (x_2 - 2)^2 \leq 0.03$ and $c_{p,0} = 0.0$, otherwise. Also, we consider $c_{l,0} = 0.003$, $\phi_0 = 0.2$ and $p_0 = 0$ in the entire domain. Figure 6 presents the results of a localised oedema formation. Each row presents snapshots of the variables c_p, c_l, p, $\boldsymbol{u}$ and ϕ_f, respectively, at three selected time instants.

The dynamics of the immune response can be observed in Fig. 6 in terms of c_p and c_l. After the pathogens appear in the tissue, they start to grow (Fig. 6 at time $t = 8$ days) and reach their peak concentration (Fig. 6 at time $t = 13$ days). However, in response to these events, leukocytes migrate to the infected site and their concentration also grows (Fig. 6, c_l column). As a consequence of the presence of leukocytes, pathogen concentration starts to decrease, as Fig. 6 shows for c_l at time $t = 18$ days.

The presence of pathogens triggers a mechanical response due to a sequence of couplings in the model. The endothelium increases its permeability to allow leukocytes to leave the bloodstream and enter the tissue. This increase in the endothelium permeability in turn increases interstitial fluid and pressure (Fig. 6 for ϕ_f and p at time $t = 8$ days). When the concentration of pathogens reaches its peak (Fig. 6 for c_p at time $t = 13$ days), it is possible to observe that the amount of fluid phase ϕ_f in the tissue also reaches its maximum value. An increase of liquid in the region leads to an increase in both pressure and displacement fields (Fig. 6 for $\boldsymbol{u}$ and p at time $t = 13$ days). Finally, when pathogens c_p are almost eliminated by the leukocytes at time $t = 18$ days, the dynamics of pressure, fluid phase fraction and displacements, tend to return to their initial values.
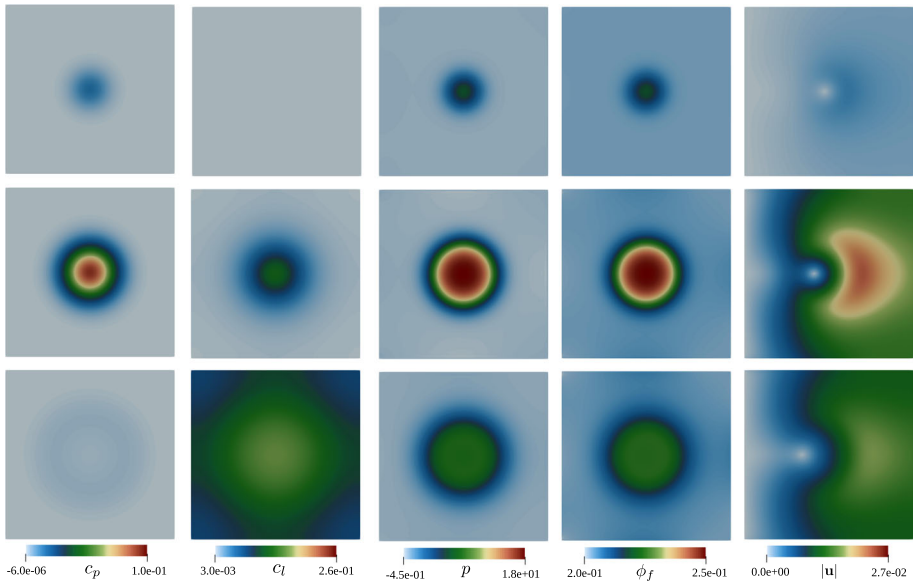
-6.0e-06 c_p 1.0e-01   3.0e-03 c_l 2.6e-01   -4.5e-01 p 1.8e+01   2.0e-01 ϕ_f 2.5e-01   0.0e+00 $|\boldsymbol{u}|$ 2.7e-02

Fig. 6 Example 4. Behaviour of pathogen (first column) and leukocyte (second column) concentrations, pressure field (third column), fraction of fluid phase (fourth column) and displacement field (fifth column) at time $t = 8$ (top row), $t = 13$ (middle row) and $t = 18$ (bottom row), after the solution of the model (2.2a)–(2.2c) and (2.4a)–(2.4b), considering the parameters given by Table 1 and initial conditions given by $c_{p,0} = 0.001$, $c_{l,0} = 0.003$, $\phi_0 = 0.2$, $\boldsymbol{u}_0 = \boldsymbol{0}$, and $p_0 = 0$

6.5 Example 5: Immune System Dynamics and Poro-hyperelasticity in a Left Ventricle

Next we conduct a series of tests using a ventricular geometry segmented from patient-specific images [78], and where synthetic muscle fibre and collagen sheet directions are constructed using a Laplace–Dirichlet rule-based method [66]. On the basal surface we prescribe zero normal displacement and zero fluid pressure flux, the epicardium is considered stress-free and with a prescribed fluid pressure, and on the endocardium we impose a time-dependent traction $\boldsymbol{t}_\Sigma = m_0 \sin^2(\pi t)\boldsymbol{n}$ with $m_0 = 0.1\,\text{N/cm}^2$, and an endocardial fluid pressure $p_{\text{endo}} = p_0 \sin^2(\pi t)$ having the same time period. No-flux conditions are used for the concentrations on the whole boundary.

For this example we use the Holzapfel–Ogden constitutive strain energy stated in (2.1), and employ the anisotropic Kozeny–Carman permeability κ^{KC} introduced in (2.3); while the remaining model parameters used for the 3D ventricular test assume the values

$$\lambda_s = 27.293\,\text{kPa}, \quad \mu_s = 3.103\,\text{kPa}, \quad \mathbf{D}_p = 3 \times 10^{-3}/\phi_0\,\text{cm}^2/\text{h}\,\mathbf{I}$$
$$\pi_i = 10\,\text{mmHg}, \quad n = 5, \quad \alpha = 0.5,$$
$$\mathbf{D}_l = 5 \times 10^{-2}/\phi_0\,\text{cm}^2/\text{h}\,\mathbf{I} \quad v_{\max} = 20, \quad \sigma_0 = 0.91, \quad \phi_0 = 0.2,$$
$$p_0 = 10.9\,\text{mmHg}, \quad k_m = 6.5\,\text{mmHg},$$
$$\pi_c = p_c = 20\,\text{mmHg}, \quad S/V = 174, \quad \chi = 10^{-4}\,\text{cm}^3/(\text{h}.10^7\text{cell}),$$
$$\gamma_p = 0.13/\phi_0\,\text{cm}^3/(\text{h}.10^7\text{cell}),$$
$$\lambda_{pl} = 7.1/\phi_0, \quad \lambda_{lp} = 1.8/\phi_0, \quad l_0 = 0\,\text{cm/s}, \quad L_{bp} = 5000,$$
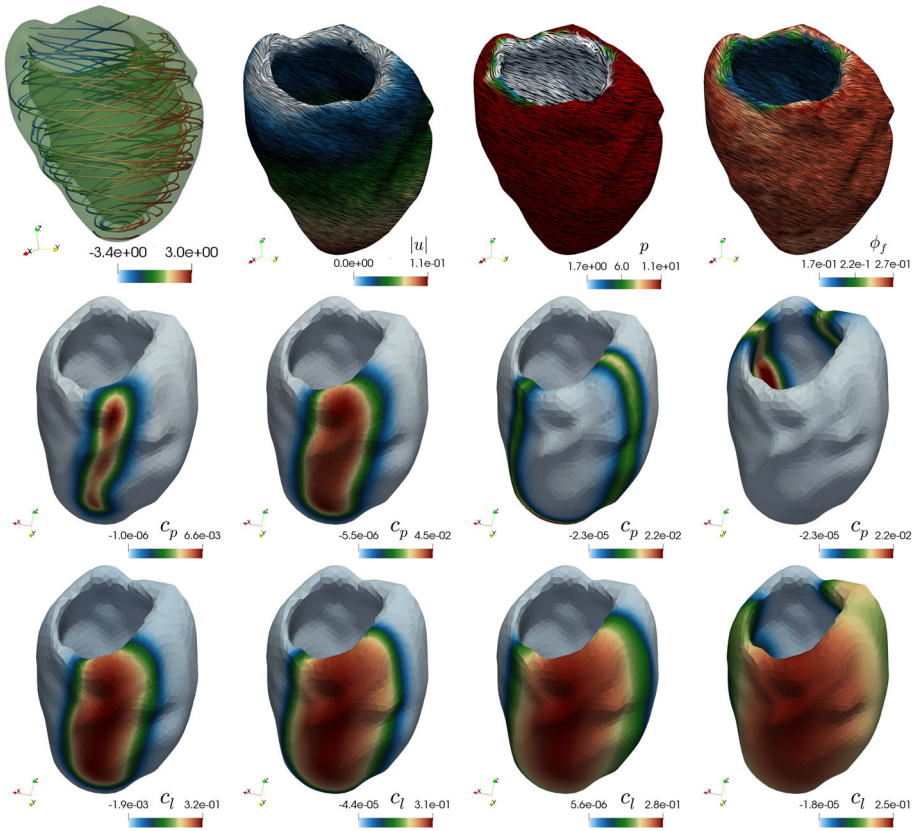
Fig. 7 Example 5. Assigned fibre distribution streamlines, displacement magnitude, fluid pressure distribution, and porosity on a patient-specific left ventricular geometry at $t = 14$ (top), and evolution of pathogens and leukocytes concentration (middle and bottom rows, respectively, seen from a slightly different angle)

$$L_{p0} = 3.6 \times 10^{-8}, \quad \mu_f = 10^{-3} \, \text{cm}^2/\text{s},$$
$$\kappa_0 = 2.5 \times 10^{-7} \, \text{cm}^2, \quad \rho_s = 2 \times 10^{-3} \, \text{Kg/cm}^3, \quad \rho_f = 10^{-3} \, \text{Kg/cm}^3,$$
$$a = 0.496 \, \text{N/cm}^2, \quad b = 0.041,$$
$$a_f = 0.193 \, \text{N/cm}^2, \quad b_f = 0.176, \quad a_s = 0.123 \, \text{N/cm}^2, \quad b_s = 0.209,$$
$$a_{fs} = 0.162 \, \text{N/cm}^2, \quad b_{fs} = 0.166.$$

An initial concentration of pathogens is considered on a transmural strip, and we simulate the dynamical behaviour of the coupled system over several minutes. The evolution of the pathogens and leukocytes distribution on the deformed ventricular geometry is shown in Fig. 7, where we also show fibre distribution and mechanical fields at half-time. One can observe that the presence of pathogens induces the local entry of leukocytes. Fluid also enters the interstitial space of the tissue, increasing pressure. Although leukocytes can remove part of the pathogens, some of them diffuse through almost the entire domain. As this pathogens' wave sweeps a significant part of the left ventricle, more parts of the heart are impacted by the inflammatory response and, as a consequence, diffuse oedema is formed. Numerical simulations show that the propagation of the front of pathogens likely depends on the diffusion

Table 2 Example 5. Iteration counts, total and (average), for fGMRES with the proposed preconditioner, and for either continuous and piecewise linear approximations of displacement, or piecewise linear displacements with bubble enrichment

DoFs	1 cpu	2 cpu	4 cpu	8 cpu	16 cpu	32 cpu
(a) Displacement approximated with $\mathbb{P}_1$ elements						
28924	48 (6.86)	88 (12.57)	81 (11.57)	87 (12.43)	80 (11.43)	90 (12.86)
155351	74 (6.73)	139 (12.64)	122 (12.20)	103 (12.88)	89(12.71)	93 (13.29)
(b) Displacement approximated with $\mathbb{P}_1^b$ elements						
72772	74 (6.73)	139 (12.64)	122 (12.20)	103 (12.88)	89 (12.71)	93 (13.29)
438158	50 (6.25)	88 (11.00)	83 (11.86)	85 (10.62)	77 (11.00)	80 (11.43)

Note that an increase in the total iterations, for constant average iterations, occurs due to a different number of Newton iterations

and replication of pathogens and the wave tail likely depends on the diffusion and efficiency of the leukocytes [52]. The numerical results indicate that, although fluid phase and pressure increase due to the presence of the pathogen, they result in small changes in displacement. In fact, new diagnostic tools have been studied to increase the non-invasive diagnostic accuracy of myocarditis and other myocardial pathologies using for this purpose the detection of increased water contents at some regions instead of an increase in tissue displacement. See, for example, [47, 72, 73].

To conclude this section, for the ventricular geometry we proceed to briefly test the preconditioner described in Sect. 5.2. To measure its performance, we look at the total and average number of Krylov iterations in two different meshes corresponding to the left ventricle geometry and with respect to $\mathbb{P}_1$ and $\mathbb{P}_1^{pb}$ (bubble enriched element) conforming finite elements for the displacement to study the impact of the inf-sup stability in the performance. The results are shown in Table 2, and as we have observed that numerically the most difficult time instant is the first one, we report the performance only on it.

We highlight that the number of average Krylov iterations is roughly constant with an increasing number of cores. This can be expected due to the use of inexact solvers in the sub-blocks of the Schur complement preconditioner, which yield an adequate approximation of the exact Schur preconditioner, which has at most 3 distinct eigenvalues. It is particularly interesting to observe that this performance is obtained by using only the action of an AMG preconditioner for the chemotaxis block, meaning that (i) the coupling between the chemotaxis and poroelastic models is not very strong in passive cardiac simulations and that (ii) such block is not necessarily computationally challenging.

7 Final Remarks

We have studied a general model capturing the phenomenological features of the interaction between chemotaxis of the immune system in saturated poroelastic media admitting large deformations. The essential properties of the new model include a formulation in terms of displacement, fluid pressure, and Lagrangian porosity, coupled with concentrations for leukocytes and pathogens. In particular, the poro-hyperelastic compartment of the model can be identified, after linearisation and adequately choosing the initial guess, with the three-field formulation for Biot's poroelasticity from [60, 77]. We have proposed a finite element method together with splitting strategies, and have studied their properties in terms of accuracy and

iteration count. The realisation of the coupling is general enough to accommodate different types of model specifications, including diverse hyperelastic solid laws and showing the interplay of solid deformation, effective stress, and pore fluid pressure build-up. The model also includes species transport through the total velocity, and the system is solved by means of a monolithic finite element method in saddle-point form.

Some extensions in the development of this work include the study of long-term behaviour of the oedema formation, as well as performing a thorough exploration of different effects from introducing lymphatic sinks for c_p and c_l. We also plan to incorporate active stress due to calcium release (in turn generated by the immune reaction-diffusion) and assess quantitative differences in the classical diffusion case. In a more applicative context, a more comprehensive sensitivity analysis is still required to determine the most relevant coupling mechanisms. Also, the validation and verification of the model against patient-specific data are still to be conducted. We have expanded the application discussed in Sect. 6.5 to address further modelling and numerically oriented investigations in the recent work [52]. Regarding numerical schemes, a possible next step is to use mixed formulations for the immune system equations (following, e.g., [43]) to produce mass conservative discretisations.

Further investigation is necessary, for instance, regarding the specific form of the anisotropic porosity as well as in designing new coupling mechanisms that will contribute to a better understanding of the formation and termination of myocarditis and myocardial oedema.

Data Availibility Part of the datasets and finite element implementations generated during and/or analysed during the current study are available from the `GitHub` repository https://github.com/ruizbaier/PoroelasticModelForAcuteMyocarditis.

Declarations

Conflict of interest The authors declare that the research was conducted in the absence of any commercial or financial relationships that could be construed as a potential conflict of interest.

References

1. Alnæs, M.S., Blechta, J., Hake, J., Johansson, A., Kehlet, B., Logg, A., Richardson, C., Ring, J., Rognes, M.E., Wells, G.N.: The FEniCS project version 1.5. Arch. Numer. Softw. **3**, 9–23 (2015)
2. Alves, J.R., de Queiroz, R.A.B., Bär, M., dos Santos, R.W.: Simulation of the perfusion of contrast agent used in cardiac magnetic resonance: a step toward non-invasive cardiac perfusion quantification. Front. Physiol. **10**, 177 (2019)
3. Alves, J.R., de Queiroz, R.A.B., Weber dos Santos, R.: Simulation of cardiac perfusion by contrast in the myocardium using a formulation of flow in porous media. J. Comput. Appl. Math. **295**, 13–24 (2016)
4. Amestoy, P.R., Duff, I.S., L'Excellent, J.-Y., Koster, J.: MUMPS: a general purpose distributed memory sparse solver, In: International Workshop on Applied Parallel Computing, Springer, pp. 121–130, (2000)
5. Anaya, V., Bendahmane, M., Mora, D., Ruiz-Baier, R.: On a vorticity-based formulation for reaction-diffusion-brinkman systems. Netw. Heterog. Media **13**, 69–94 (2018)
6. Arnold, D.N., Brezzi, F., Fortin, M.: A stable finite element for the Stokes equations. Calcolo **21**, 337–344 (1984)
7. Ateshian, G.A., Weiss, J.A.: Anisotropic hydraulic permeability under finite deformation. J. Biomech. Eng. **132**, 111004(7) (2010)
8. Auricchio, F., Beirão da Veiga, L., Lovadina, C., Reali, A.: A stability study of some mixed finite elements for large deformation elasticity problems. Comput. Methods Appl. Mech. Eng. **194**, 1075–1092 (2005)
9. Bærland, T., Lee, J.J., Mardal, K.-A., Winther, R.: Weakly imposed symmetry and robust preconditioners for Biot's consolidation model. Comput. Methods Appl. Math. **17**, 377–396 (2017)
10. Barnafi, N., De Oliveira Vilaca, L.M., Milinkovitch, M.C., Ruiz-Baier, R.: Coupling chemotaxis and poromechanics for the modelling of feather primordia patterning, In preparation, pp. 1–28, (2021)
11. Barnafi, N., Di Gregorio, S., Dede', L., Zunino, P., Vergara, C., Quarteroni, A.M.: A multiscale poromechanics model integrating myocardial perfusion and systemic circulation, MOX Reports (2021)
12. Barnafi, N., Zunino, P., Dedè, L., Quarteroni, A.: Mathematical analysis and numerical approximation of a general linearized poro-hyperelastic model. Comput. Math. Appl. **91**, 202–228 (2021)
13. Basser, P.J.: Interstitial pressure, volume, and flow during infusion into brain tissue. Microvasc. Res. **44**, 143–165 (1992)
14. Berger, L., Bordas, R., Burrowes, K., Grau, V., Tavener, S., Kay, D.: A poroelastic model coupled to a fluid network with applications in lung modelling. Int. J. Numer. Methods Biomed. Eng. **32**, e02731 (2016)
15. Berger, L., Bordas, R., Kay, D., Tavener, S.: A stabilized finite element method for finite-strain three-field poroelasticity. Comput. Mech. **60**, 51–68 (2017)
16. Borregales, M., Radu, F.A., Kumar, K., Nordbotten, J.M.: Robust iterative schemes for non-linear poromechanics. Comput. Geosci. **22**, 1021–1038 (2018)
17. Both, J., Borregales, M., Nordbotten, J., Kumar, K., Radu, F.: Robust fixed stress splitting for Biot's equations in heterogeneous media. Appl. Math. Lett. **68**, 101–108 (2017)
18. Both, J., Kumar, K., Nordbotten, J., Radu, F.: The gradient flow structures of thermo-poro-visco-elastic processes in porous media, arXiv e-prints (2019)
19. Both, J.W., Barnafi, N.A., Radu, F.A., Zunino, P., Quarteroni, A.: Iterative splitting schemes for a soft material poromechanics model. Comput. Methods Appl. Mech. Eng. **388**, e114183 (2022)
20. Brenner, S.C., Scott, L.R.: The mathematical theory of finite element methods. Texts in Applied Mathematics, Springer, New York (2002)
21. Burger, R.L., Belitz, K.: Measurement of anisotropic hydraulic conductivity in unconsolidated sands: a case study from a shoreface deposit, Oyster, Virginia. Water Resources Res. **33**, 1515–1522 (1997)
22. Burtschell, B., Chapelle, D., Moireau, P.: Effective and energy-preserving time discretization for a general nonlinear poromechanical formulation. Comput. Struct. **182**, 313–324 (2017)
23. Chamberland, E., Fortin, A., Fortin, M.: Comparison of the performance of some finite element discretizations for large deformation elasticity problems. Comput. Struct. **88**, 664–673 (2010)
24. Chapelle, D., Gerbeau, J.-F., Sainte-Marie, J., Vignon-Clementel, I.E.: A poroelastic model valid in large strains with applications to perfusion in cardiac modeling. Comput. Mech. **46**, 91–101 (2010)
25. Chapelle, D., Moireau, P.: General coupling of porous flows and hyperelastic formulations - from thermodynamics principles to energy balance and compatible time schemes. Eur. J. Mech., B/Fluids **46**, 82–96 (2014)
26. Cherubini, C., Filippi, S., Gizzi, A., Ruiz-Baier, R.: A note on stress-driven anisotropic diffusion and its role in active deformable media. J. Theor. Biol. **430**, 221–228 (2017)
27. Choo, J.: Large deformation poromechanics with local mass conservation: an enriched Galerkin finite element framework. Int. J. Numer. Methods Eng. **116**, 66–90 (2019)

28. Cioncolini, A., Boffi, D.: The MINI mixed finite element for the Stokes problem: An experimental investigation. Comput. Math. Appl. **77**, 2432–2446 (2019)
29. Colli Franzone, P., Pavarino, L.F., Scacchi, S.: Mathematical Cardiac Electrophysiology, vol. 13. Springer, Berlin (2014)
30. Cookson, A., Lee, J., Michler, C., Chabiniok, R., Hyde, E., Nordsletten, D., Sinclair, M., Siebes, M., Smith, N.: A novel porous mechanical framework for modelling the interaction between coronary perfusion and myocardial mechanics. J. Biomech. **45**, 850–855 (2012)
31. Coussy, O.: Poromechanics. Wiley, New York (2004)
32. De Oliveira Vilaca, L.M., Gómez-Vargas, B., Kumar, S., Ruiz-Baier, R., Verma, N.: Stability analysis for a new model of multi-species convection-diffusion-reaction in poroelastic tissue. Appl. Math. Model. **84**, 425–446 (2020)
33. Deparis, S., Forti, D., Grandperrin, G., Quarteroni, A.: FaCSI: A block parallel preconditioner for fluid-structure interaction in hemodynamics. J. Comput. Phys. **327**, 700–718 (2016)
34. Ehret, A.E., Bircher, K., Stracuzzi, A., Marina, V., Zündel, M., Mazza, E.: Inverse poroelasticity as a fundamental mechanism in biomechanics and mechanobiology. Nature Comm. **10**, e1002 (2017)
35. Elman, H., Howle, V.E., Shadid, J., Shuttleworth, R., Tuminaro, R.: A taxonomy and comparison of parallel block multi-level preconditioners for the incompressible Navier–Stokes equations. J. Comput. Phys. **227**, 1790–1808 (2008)
36. Farrell, P.E., Gatica, L.F., Lamichhane, B.P., Oyarzúa, R., Ruiz-Baier, R.: Mixed Kirchhoff stress - displacement - pressure formulations for incompressible hyperelasticity. Comput. Methods Appl. Mech. Eng. **374**, e113562 (2021)
37. Federico, S., Herzog, W.: On the anisotropy and inhomogeneity of permeability in articular cartilage. Biomech. Model. Mech. **7**, 367–378 (2007)
38. Franceschini, A., Castelletto, N., Ferronato, M.: Approximate inverse-based block preconditioners in poroelasticity. Comput. Geosci. **25**, 701–714 (2021)
39. Freitas Reis, R., Fernandes, J.L., Schmal, T.R., Martins Rocha, B., Weber Dos Santos, R., Lobosco, M.: A personalized computational model of edema formation in myocarditis based on long-axis biventricular MRI images. BMC Bioinform. **20**, 532(11) (2019)
40. Freitas Reis, R., Weber Dos Santos, R., Martins Rocha, B., Lobosco, M.: On the mathematical modeling of inflammatory edema formation. Comput. Math. Appl. **78**, 2994–3006 (2019)
41. Friedrich, M.G., Sechtem, U., Schulz-Menger, J., Holmvang, G., Alakija, P., Cooper, L.T., White, J.A., Abdel-Aty, H., Gutberlet, M., Prasad, S., Aletras, A., Laissy, J.-P., Paterson, I., Filipchuk, N.G., Kumar, A., Pauschinger, M., Liu, P.: Cardiovascular magnetic resonance in myocarditis: a JACC white paper. J. Am. College Cardiology **53**, 1475–1487 (2009)
42. Frigo, M., Castelletto, N., Ferronato, M.: A relaxed physical factorization preconditioner for mixed finite element coupled poromechanics. SIAM J. Sci. Comput. **41**, B694–B720 (2019)
43. Gatica, G.N., Oyarzúa, R., Ruiz-Baier, R., Sobral, Y.D.: Banach spaces-based analysis of a fully-mixed finite element method for the steady-state model of fluidized beds. Comput. Math. Appl. **84**, 244–276 (2021)
44. Girault, V., Raviart, P.-A.: Finite Element Approximation of the Navier–Stokes Equation. Lecture Notes in Math, vol. 749. Springer, Berlin (1979)
45. Holzapfel, G.A., Ogden, R.W.: Constitutive modelling of passive myocardium: a structurally based framework for material characterization. Phil. Trans. Royal Soc. Lond. A **367**, 3445–3475 (2009)
46. Hong, Q., Kraus, J., Lymbery, M., Philo, F.: Conservative discretizations and parameter-robust preconditioners for biot and multiple-network flux-based poroelasticity models. Numer. Linear Algebra Appl. **26**, e2242 (2019)
47. Kim, P.K., Hong, Y.J., Im, D.J., Suh, Y.J., Park, C.H., Kim, J.Y., Chang, S., Lee, H.-J., Hur, J., Kim, Y.J., et al.: Myocardial t1 and t2 mapping: techniques and clinical applications. Korean J Radiol. **18**, 113–131 (2017)
48. Kirby, R.C., Mitchell, L.: Solver composition across the PDE/linear algebra barrier. SIAM J. Scientific Comput. **40**, C76–C98 (2018)
49. Korsawe, J., Starke, G., Wang, W., Kolditz, O.: Finite element analysis of poro-elastic consolidation in porous media: Standard and mixed approaches. Comput. Methods Appl. Mech. Eng. **195**, 1096–1115 (2006)
50. Lang, G.E., Vella, D., Waters, S.L., Goriely, A.: Mathematical modelling of blood-brain barrier failure and oedema. Math. Med. Biol. **34**, 391–414 (2016)
51. Li, C., Borja, R.I., Regueiro, R.A.: Dynamics of porous media at finite strain. Comput. Methods Appl. Mech. Eng. **193**, 3837–3870 (2004)

52. Lourenço, Wd.J., Reis, R.F., Ruiz-Baier, R., Rocha, B.M., Weber dos Santos, R., Lobosco, M.: A poroelastic approach for modelling myocardial oedema in acute myocarditis. Front. Physiol. **13**, e888515(1-14) (2022)

53. MacMinn, C.W., Dufresne, E.R., Wettlaufer, J.S.: Large deformations of a soft porous material. Phys. Rev. Appl. **5**, 044020(30) (2016)

54. Mauck, R.T., Hung, C.T., Ateshian, G.A.: Modelling of neutral solute transport in a dynamically loaded porous permeable gel: implications for articular cartilage biosynthesis and tissue engineering. J. Biomech. Eng. **125**, 602–614 (2003)

55. Mikelić, A., Wheeler, M.F.: Convergence of iterative coupling for coupled flow and geomechanics. Comput. Geosci. **17**, 455–461 (2013)

56. Moeendarbary, E., Valon, L., Fritzsche, M., Harris, A.R., Mouling, D.A., Thrasher, A.J., Stride, E., Mahadevan, L., Charras, G.T.: The cytoplasm of living cells behaves as a poroelastic material. Nat. Mater. **12**, 3517 (2013)

57. Murphy, M.F., Golub, G.H., Wathen, A.J.: A note on preconditioning for indefinite linear systems. SIAM J. Sci. Comput. **21**, 1969–1972 (2000)

58. Nash, M.P., Hunter, P.J.: Computational mechanics of the heart. From tissue structure to ventricular function. J. Elast. **61**, 113–141 (2000)

59. Nedjar, B.: Formulation of a nonlinear porosity law for fully saturated porous media at finite strains. J. Mech. Phys. Solids **61**, 537–556 (2013)

60. Oyarzúa, R., Ruiz-Baier, R.: Locking-free finite element methods for poroelasticity. SIAM J. Numer. Anal. **54**, 2951–2973 (2016)

61. Phipps, C., Kohandel, M.: Mathematical model of the effect of interstitial fluid pressure on angiogenic behavior in solid tumors. Comput. Math. Methods Med. **2011**, e.843765 (2011)

62. Puntmann, V.O., Zeiher, A.M., Nagel, E.: T1 and T2 mapping in myocarditis: seeing beyond the horizon of Lake Louise criteria and histopathology. Expert Rev. Cardiovasc. Therapy **16**, 319–330 (2018)

63. Quarteroni, A., Lassila, T., Rossi, S., Ruiz-Baier, R.: Integrated heart - coupled multiscale and multiphysics models for the simulation of the cardiac function. Comput. Methods Appl. Mech. Eng. **314**, 345–407 (2017)

64. Quarteroni, A., Valli, A.: Numerical Approximation of Partial Differential Equations. Springer Series in Computational Mathematics, vol. 23. Springer, Berlin (1994)

65. Rohan, E., Lukeš, V.: Modeling large-deforming fluid-saturated porous media using an Eulerian incremental formulation. Adv. Eng. Softw. **113**, 84–95 (2017)

66. Rossi, S., Lassila, T., Ruiz-Baier, R., Sequeira, A., Quarteroni, A.: Thermodynamically consistent orthotropic activation model capturing ventricular systolic wall thickening in cardiac electromechanics. Eur. J. Mech.: A/Solids **48**, 129–142 (2014)

67. Ruiz-Baier, R.: Primal-mixed formulations for reaction-diffusion systems on deforming domains. J. Comput. Phys. **299**, 320–338 (2015)

68. Saad, Y.: A flexible inner-outer preconditioned GMRES algorithm. SIAM J. Sci. Comput. **14**, 461–469 (1993)

69. Saad, Y., Schultz, M.H.: GMRES: A generalized minimal residual algorithm for solving nonsymmetric linear systems. SIAM J. Sci. Statist. Comput. **7**, 856–869 (1986)

70. Sacco, R., Causin, P., Lelli, C., Raimondi, M.T.: A poroelastic mixture model of mechanobiological processes in biomass growth: theory and application to tissue engineering. Meccanica **52**, 3273–3297 (2017)

71. Showalter, R.E.: Poroelastic filtration coupled to Stokes flow, In: Control Theory of Partial Differential Equations, O. Imanuvilov, G. Leugering, R. Triggiani, and B.-Y. Zhang, eds., vol. 242 of Lecture Notes in Pure and Applied Mathematics, Chapman & Hall, Boca Raton, 2005, pp. 229–241

72. Spieker, M., Haberkorn, S., Gastl, M., Behm, P., Katsianos, S., Horn, P., Jacoby, C., Schnackenburg, B., Reinecke, M., Kelm, M., et al.: Abnormal t2 mapping cardiovascular magnetic resonance correlates with adverse clinical outcome in patients with suspected acute myocarditis. J. Cardiovasc. Magn. Resonance **19**, 38 (2017)

73. Spieker, M., Katsianos, E., Gastl, M., Behm, P., Horn, P., Jacoby, C., Schnackenburg, B., Reinecke, P., Kelm, M., Westenfeld, R., et al.: T2 mapping cardiovascular magnetic resonance identifies the presence of myocardial inflammation in patients with dilated cardiomyopathy as compared to endomyocardial biopsy. Eur. Heart J.-Cardiovasc. Imaging **19**, 574–582 (2017)

74. Sundnes, J., Lines, G.T., Cai, X., Nielsen, B.F., Mardal, K.-A., Tveito, A.: Computing the Electrical Activity in the Heart, vol. 1. Springer, Berlin (2007)

75. Thompson, T.B., Rivière, B.M., Knepley, M.G.: An implicit discontinuous Galerkin method for modeling acute edema and resuscitation in the small intestine. Math. Med. Biol. **36**, 513–548 (2019)

76. van Furth, R., Cohn, Z.A.: The origin and kinetics of mononuclear phagocytes. J. Exp. Med. **128**, 415–435 (1968)

77. Verma, N., Gómez-Vargas, B., De Oliveira Vilaca, L. M., Kumar, S., Ruiz-Baier, R.: Well-posedness and discrete analysis for advection-diffusion-reaction in poroelastic media, Applicable Analysis, in press (2021)

78. Warriner, D.R., Jackson, T., Zacur, E., Sammut, E., Sheridan, P., Hose, D.R., Lawford, P., Razavi, R., Niederer, S.A., Rinaldi, C.A., Lamata, P.: An asymmetric wall-thickening pattern predicts response to cardiac resynchronization therapy. JACC: Cardiovasc. Imag. **11**, 1545–1546 (2018)

79. White, J., Castelletto, N., Tchelepi, H.: Block-partitioned solvers for coupled poromechanics: A unified framework. Comput. Methods Appl. Mech. Eng. **303**, 55–74 (2016)

80. White, J.A., Castelletto, N., Klevtsov, S., Bui, Q.M., Osei-Kuffuor, D., Tchelepi, H.A.: A two-stage preconditioner for multiphase poromechanics in reservoir simulation. Comput. Methods Appl. Mech. Eng. **357**, 112575 (2019)

81. Yang, U.M., Henson, V.E.: BoomerAMG: a parallel algebraic multigrid solver and preconditioner. Appl. Numer. Math. **41**, 155–177 (2002)

82. Young, J., Rivière, B.M., Cox, C.S., Uray, K.: A mathematical model of intestinal oedema formation. Math. Med. Biol. **31**, 1–15 (2012)

83. Yu, C., Malakpoor, K., Huyghe, J.M.: A mixed hybrid finite element framework for the simulation of swelling ionized hydrogels. Comput. Mech. **63**, 835–852 (2019)

84. Zheng, P., Jiao, G., Zhang, K.: A mixed stabilized finite element formulation for finite deformation of a poroelastic solid saturated with a compressible fluid, Arch. Appl. Mech., in press, pp. 1–19, (2020)

85. Zheng, P., Zhang, K.: On the effective stress law and its application to finite deformation problems in a poroelastic solid. Int. J. Mech. Sci. **161–162**, e105074 (2019)

Authors and Affiliations

N. A. Barnafi[1] [ID] · **B. Gómez-Vargas[2]** [ID] · **W. J. Lourenço[3]** · **R. F. Reis[3]** · **B. M. Rocha[3]** [ID] · **M. Lobosco[3]** · **R. Ruiz-Baier[4,5,6]** [ID] · **R. Weber dos Santos[3]** [ID]

N. A. Barnafi
nicolas.barnafi@unimi.it

B. Gómez-Vargas
bryan.gomezvargas@ucr.ac.cr

W. J. Lourenço
wesleydejesuspearl@ice.ufjf.br

R. F. Reis
ruyfreitas@ice.ufjf.br

B. M. Rocha
bernardomartinsrocha@ice.ufjf.br

M. Lobosco
marcelo.lobosco@ice.ufjf.br

R. Weber dos Santos
rodrigo.weber@ufjf.edu.br

[1]   Department of Mathematics "Federigo Enriques", Università degli Studi di Milano, Via Saldini 50, 20133 Milan, Italy

[2]   Sección de Matemática, Sede de Occidente, Universidad de Costa Rica, San Ramón de Alajuela, Costa Rica

[3]   Graduate Program on Computational Modeling, Federal University of Juiz de Fora, Rua José LourençoKelmer, s/n - São Pedro, 36036-900 Juiz de Fora, MG, Brazil

[4]   School of Mathematical Sciences and Victorian Heart Institute, Monash University, 9 Rainforest Walk, Melbourne, VIC 3800, Australia

[5]   World-Class Research Center "Digital biodesign and personalized healthcare", Sechenov First Moscow State Medical University, Moscow, Russia

[6]   Universidad Adventista de Chile, Casilla 7-D, Chillán, Chile